

POLITECNICO DI TORINO

Corso di Laurea Magistrale in Ingegneria Aerospaziale

Tesi di Laurea Magistrale

Innovative structures for vibration control



**Politecnico
di Torino**

Relatori

prof. Erasmo Carrera
prof. Alfonso Pagani
dr. Matteo Filippi

Candidato

Riccardo Salgarella

Anno Accademico 2020/2021

Ringraziamenti

Innanzitutto vorrei ringraziare i miei genitori che con pazienza mi hanno supportato fino al raggiungimento di questo importante traguardo. Vi ringrazio per aver chiamato ogni giorno, anche se non me la sentivo di parlare. Vi ringrazio per avermi dato la libertà di percorrere i miei sogni senza preoccupazioni. Ringrazio i nonni, gli zii, le zie e tutte le persone che hanno seguito il mio percorso fin dai primi passi. Ringrazio gli amici e compagni che hanno reso le serate di quarantena piacevoli pur senza poter uscire di casa e che tuttora continuano a rendere le giornate molto più interessanti. Un ringraziamento speciale alle persone che hanno reso possibile questa tesi, presentandomi l'opportunità in un periodo di incertezza e aiutandomi a comprendere meglio una lingua che non è mia.

Abstract

Metamaterials are a recent development of material science and they are designed to have specific properties not common for classical materials. Lattice materials are a class of materials characterised by being made of a repetition of cells in one or more directions to achieve a more optimised distribution of the load on the structure. By bonding these two definitions, a new class of materials is created that uses the repetition of cells to make a new material able to absorb vibrations while being able to be deployed on a wide range of application, from insulation to aerospace. The objective of this dissertation is to analyse various type of cells using the Carrera Unified Formulation (CUF) package and the Wave Finite Element Method (WFEM) to assess the performance of those structures and propose new ones that can be used as vibration control medium.

The first part of this document is focused on the study of the proposed structure with the tools for eigenvalue analysis built-in on the CUF package. The second part is mostly dedicated to the use of the WFEM for the solution of the wave propagation problem to study the performance of various structures.

Contents

List of Tables	6
List of Figures	7
I Introduction	10
Introduction	11
0.1 Metamaterials and lattice structures	11
0.2 Structural Theories	11
0.3 Carrera Unified Formulation	12
0.3.1 Derivation of a FE beam with CUF	13
0.4 Structure of the thesis	14
1 Geometry characterization	16
1.1 Introduction	16
1.1.1 Discretizations	16
1.1.2 Boundary conditions	19
1.2 Free vibration analysis	19
1.2.1 Gate frequencies deviation	19
1.2.2 Shear locking	20
1.2.3 3D structure frequencies analysis	22
1.2.4 Configurations analysis	23
2 Material characterization	27
2.1 Introduction	27

2.2	Materials selection	28
2.2.1	Combination	28
2.3	Simulation	29
2.3.1	Materials selection	29
2.3.2	Materials distribution	31
II	Wave analysis	35
3	Wave propagation problem	36
3.1	Introduction	36
3.1.1	WFE Theory	38
3.1.2	Case studies	40
4	Wave propagation analysis	59
4.1	Proposed configurations	59
4.1.1	Option 1 - TE discretisation	61
4.1.2	Option 2 - 2D gate structure	61
4.1.3	Option 3 - 3D cube structure	63
4.2	Cube core sandwich panel	63
4.2.1	Results with Taylor Expansion	69
III	Conclusions	84
4.3	Characterisation	85
4.4	Wave propagation problem	86

List of Tables

1.1	Gate analysis results table [Hz]	25
1.2	Tridimensional structure modes	26
2.1	Materials used in the study	27
2.2	Addictive Manufacturing metal technique	28
2.3	Materials combination	29
3.1	Eigenvalue properties and associated wave	40
3.2	Geometrical variation of the two subcells	46
3.3	Material variation of the two subcells	50
4.1	Sandwich core materials	65
4.2	Steel core modes	73
4.3	Aluminium core modes	80
4.4	Aramid fibers core modes	83

List of Figures

1.1	Tridimensional structure with highlighted ribs (green) and spars (blue)	17
1.2	Cross-section discretizations	17
1.3	Frequencies deviation from reference (24L16)	20
1.4	Frequencies variation with shear locking compensating algorithm . .	21
1.5	Frequencies for the various configurations	22
1.6	3X3 configurations	23
2.1	1X1 configuration with highlighted ribs (blue) and spars (green) . .	30
2.2	Fitted result of the analysis on materials combinations	31
2.3	2X2 configurations	33
2.4	Frequency variation for the first six modes	34
3.1	Models used in this analysis	41
3.2	Single material cube with Lagrange expansions comparison	42
3.3	Single material cube with Taylor expansions comparison	43
3.4	Multi material cube expansions method comparison	44
3.5	Spectrum analysis with stopband shown with a blue color	45
3.6	Duble Unit cell dimensions combination	46
3.7	Super Unit cell Fibonacci sequence	46
3.8	Double Unit cell discretization	47
3.9	Duble Unit cell results with comparison with [9] (blue circles) . . .	48
3.10	Super Unit cell results with comparison with [9] (blue circles) . . .	49
3.11	Case 1 - Spectrum with highlighted stopband	51
3.12	Case 2 - Spectrum with highlighted stopband	51
3.13	Case 3 - Spectrum with highlighted stopband	52

3.14	Section view of the Configuration B beam	52
3.15	Configuration A	54
3.16	Configuration B	55
3.17	Spectrum for the TE2 discretization	56
3.18	Spectrum for the TE3 discretization	57
3.19	Spectrum for the LE9 discretization	58
4.1	Drawing of the 1X1 configuration with dimensions	60
4.2	Result of the 1X1 configuration with Taylor Expansion analysis . .	61
4.3	Drawing of the 2D configuration with dimensions	62
4.4	Result of the 2D gate analysis	63
4.5	Drawing of the Cube configuration with propagation	64
4.6	Result of the 3D cube analysis	64
4.7	Sandwich configuration	66
4.8	Result of the sandwich analysis for comparison with simple cube configuration (steel core)	67
4.9	Result of the sandwich analysis with steel core	67
4.10	Result of the sandwich analysis with aluminium core	68
4.11	Result of the sandwich analysis with aramidic fiber core	68
4.12	Result of the sandwich analysis with steel core and first-order Taylor Expansion	70
4.13	Result of the sandwich analysis with steel core and fifth-order Taylor Expansion	71
4.14	Result of the sandwich analysis with aramidic fiber core and first- order Taylor Expansion	72
4.15	Result of the sandwich analysis with aramidic fiber core and fourth- order Taylor Expansion	73
4.16	Steel modes reference graph	74
4.17	Steel modes illustration	76
4.18	Aluminium modes reference graph	77
4.19	Aluminium modes illustration	79
4.20	Aramididic modes reference graph	80
4.21	Aramididic modes illustration	83

Part I

Introduction

Introduction

0.1 Metamaterials and lattice structures

Metamaterials represent a recent class of composites introduced to identify artificially-made materials that have properties not available in natural ones, such as negative Young's module or Poisson's ratio. The first batch of research had taken into consideration the electromagnetic properties of the materials to manipulate the wavelength of an electromagnetic wave without varying its frequency. Later research has exploited the analogy between electromagnetic and acoustic waves to obtain stopbands able to absorb a specific range of frequencies. [8]

Lattice structures are constructed of interconnected unit cells tessellated in the tridimensional space, creating a periodic arrangement. Advancement in Additive Manufacturing techniques has led these structures to become more prominent in order to reduce materials usage in manufacturing, while optimizing the strength to weight ratio. Moreover, these structures can absorb energy more efficiently than whole classics structures, leading to improved vibrational dampening and isolation of sensitive areas of the construct from loaded ones. [7]

0.2 Structural Theories

Significant numbers of theories have been developed in the past centuries in order to meet the demand for an approximate solution for the structural problems. The most well known are the ones developed with the axiomatic method by eminent scientists. The axiomatic method exploits the understanding of the problem to isolate the most important mathematical terms for a given structural problem.

The resulting theories cannot be mathematically proven, but they were exploited to design most of the structures during the last few centuries. The introduction of axiomatic hypotheses on the behaviour of the unknown functions preclude the possibility to evaluate the theories accuracy, but further additional terms of the expansions can overcome this limitation and allow the engineers to work with a result which includes the precision of the theory.

As an example of axiomatic theories, the Euler-Bernoulli and Timoshenko Beam Theories (EBT and TBT) will be addressed in the next paragraphs. Firstly, the EBT embed two assumptions: the plane section remains plane and the beam slopes are small. The first assumption means any section of the beam which was a flat plane before the deformation will remain plane after the deformation. This assumption is generally valid till the beam experiences significant shear and torsional stresses relative to the bending axis. The small angle assumption allows to approximate sine and cosine. The displacements for an EBT beam are presented in Equation 1.

$$\begin{aligned}
 u &= u_0 + zw_{,x} \\
 v &= v_0 + zw_{,y} \\
 w &= w_0
 \end{aligned}
 \tag{1}$$

The TBT breaks free from the assumption and takes into consideration the shear and rotational stresses omitted for the EBT formulation. The displacements for a TBT beam are presented in Equation 2.

$$\begin{aligned}
 u &= u_0 + z\phi_x \\
 v &= v_0 + z\phi_y \\
 w &= w_0
 \end{aligned}
 \tag{2}$$

0.3 Carrera Unified Formulation

Models in this thesis will be developed via the Carrera Unified Formulation (CUF) formalism. The CUF provides monodimensional, beam, and bidimensional, plate and shell, theories more powerful than classical ones with the implementation of a condensed notation and by expressing the displacement field along the cross-

section (for beams) and the thickness (for shells and plates) using base functions with arbitrary orders and forms. The condensed notation leads to the introduction of the fundamental nucleus (FN) which consists of a few mathematical statements unrelated to the theory of structure (TOS) used. Those nuclei originate from the tridimensional elasticity equations via the principle of virtual displacement (PVD) and they can be easily obtained for the tridimensional, bidimensional and monodimensional cases. The last two cases have enhanced capabilities since they can obtain a tridimensional result with a lower computational cost. The monodimensional case emphasizes this advantage of being properly capable of deal with more complex bidimensional and tridimensional problems.[3]

In this thesis the monodimensional model will be mostly used to solve the structure.

0.3.1 Derivation of a FE beam with CUF

Tridimensional displacement field $\mathbf{u}(x, y, z, t) = (u_x, u_y, u_z)$ is approximated as:

$$\mathbf{u}(x, y, z, t) = \mathbf{u}_{i\tau}(t) \cdot N_i(y) \cdot F_\tau(x, z) \quad \tau = 1, \dots, M \quad i = 1, \dots, N_n^{1D} \quad (3)$$

where: N_i is the monodimensional Lagrangian form function, F_τ is the function used to approximate the cross sectional of the beam, $u_{i\tau}$ is the unknown coefficients vector, i is the FE index and goes from 1 to the number of nodes of the elements N_n^{1D} and τ is the index bind to the expansion used to express the cross section cynamatics and M is an input parameter for the analysis. For the analysis both Lagrange and Taylor expansions will be used and for the latter various order of expansion will be tested during the dissertation. In the cases which will be discussed in this introductory chapter, the cinematic of the cross section will be obtained with a combination of Lagrange polynomials defined inside subregions (cells) by a number of points (nodes). The number of nodes determine the order of the polynomials: four (L4) nodes for bilinear expansion, nine (L9) for trilinear expansion and sixteen (L16) for bicubic expansion. For the nine nodes cell the Interpolation functions are:

$$\begin{aligned}
F_\tau &= \frac{1}{4}(r^2 + rr_\tau)(s^2 + ss_\tau) & \tau &= 1, 3, 5, 7 \\
F_\tau &= \frac{1}{2}s_\tau^2(s^2 - ss_\tau)(1 - r^2) + \frac{1}{2}r_\tau^2(r^2 - rr_\tau)(1 - s^2) & \tau &= 2, 4, 6, 8 \\
F_\tau &= (1 - r^2)(1 - s^2) & \tau &= 9
\end{aligned} \tag{4}$$

where r and s range from -1 to 1 and r_τ and s_τ are the coordinates of the nine points on the natural reference system. The displacement field of a single L9 element is:

$$\begin{aligned}
u_x &= F_1u_{x1} + F_2u_{x2} + F_3u_{x3} + \dots + F_9u_{x9} \\
u_y &= F_1u_{y1} + F_2u_{y2} + F_3u_{y3} + \dots + F_9u_{y9} \\
u_z &= F_1u_{z1} + F_2u_{z2} + F_3u_{z3} + \dots + F_9u_{z9}
\end{aligned} \tag{5}$$

here the unknown (u_{x1}, \dots, u_{z9}) are the translational displacements of the nine points which form the element.

Layer-Wise approach

Unlike Equivalent Single Layer (ESL) techniques, where the different layers of the structure are condensed on a single virtual material with averaged properties, e.g. a composite plate, the Layer-Wise (LW) ones have different properties derived from the actual materials each layer is made of. The result of these techniques is kinematically homogeneous, so the kinematics of the individual layer is unknown. On the other hand LW theories allow the knowledge of the kinematics for each layer of the structure at the cost of introducing constraints on each interface to ensure the compatibility of the displacement components for each interface between layers. A LW approach is preferred when the structure is made of different materials and when the knowledge of the strain on the interface between layers is used e.g to evaluate the delamination of a composite plate.

0.4 Structure of the thesis

The thesis is mostly divided on two parts: the first uses the CUF package to solve the eigenproblem for each proposed structure and it is mostly focused on the study

the optimal structure to be used as a cell for the creation of a lattice metamaterial. On the other hand, the second part of the document is more focused on the study of the optimised cells embedded on a multi-cell structure, using the WFE method capacity of propagate the cell along one dimension. On the last chapter a sandwich panel, made of those structures as core, is proposed and its modes are analysed.

Chapter 1

Geometry characterization

1.1 Introduction

The following chapter will firstly address the free frequency variation of a gate-like structure with different cross-section discretizations, each with various Lagrange Expansion (LE) approximation of the subdomains, in order to identify the best trade-off between computational cost and accuracy of the results. The discretization resulting from the trade-off is then scaled to a tridimensional structure where some morphological configurations will be analysed and compared in order to identify the configuration better suited to the study of how the materials properties and distribution can change the vibrational modes of the structure.

1.1.1 Discretizations

Using the Carrera Unified Formulation (CUF) the tridimensional object is represented by means of a one-dimensional beam with the cross-sectional surface discretized with Lagrange Expansion (LE) elements to approximate.

Cross-section discretizations - 2D

The four cross-section discretizations chosen for this structure are presented on Figure 1.2. Each configuration is composed of a number of cells, every discretization has square cells on both the upper angles, but on the heads and legs various

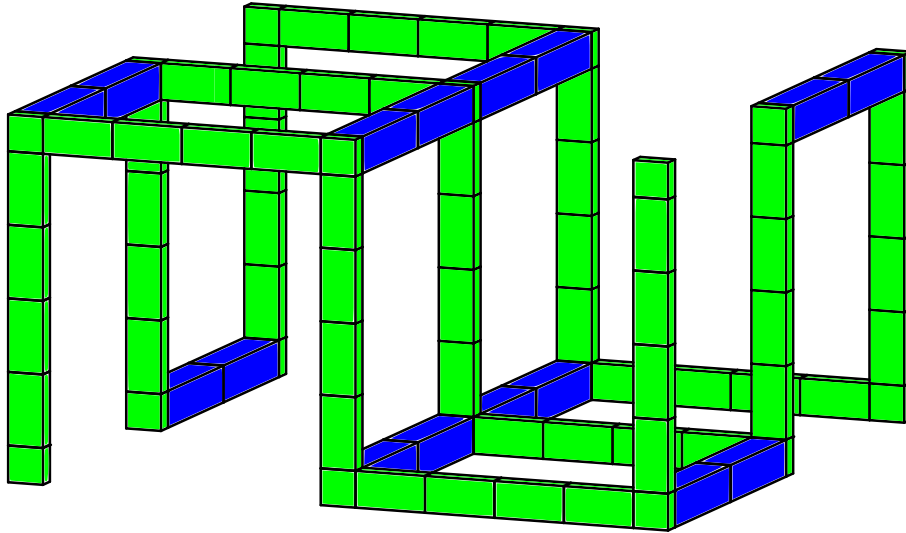


Figure 1.1: Tridimensional structure with highlighted ribs (green) and spars (blue)

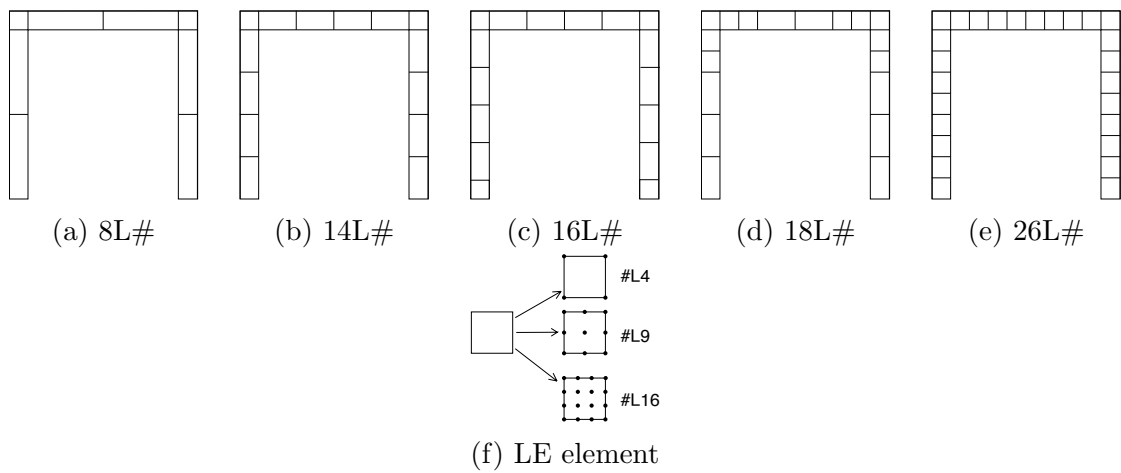


Figure 1.2: Cross-section discretizations

distributions have been tested with different meshes density and placing additional cells around the most significant part of the structure.

Each mesh configuration can be populated with different discretizations, all based on the Lagrange Expansion. In particular, discretizations with four nodes (L4), nine nodes (L9) and twelve nodes (L12) will be analyzed.

Configuration 1.2d is the most notable, with mesh thickening near the corners. Configuration 1.2e is the most time consuming, with its 3792 degrees of freedoms (DoF).

Depth discretization - 2D

Single gate-like object depth discretization is made with a single B4 element. This model has been chosen for the capability to seize the shear [TBA]. This discretization is the same for all the bidimensional configurations and will be also used on the tridimensional discretization for the gates.

Cross-section discretizations - 3D

The tridimensional cross-sectional discretization is achieved with the assembly of more gate-like linked using horizontal connective elements as the head of the gate-like cross-sectional discretization. In order to smooth and simplify this process, the configuration in Figure 1.2c is added to the analysis for validation.

Depth discretization - 3D

The various ribs, composed of repetitions of the gate-like structure and the connecting amongst each gate, are linked between them with beams discretized with two B4 elements. These beams are located on the angles and extremities of the ribs, where the cell is squared. One more configuration are achieved removing some spars from the angles of the gate-like structure in order to create series of table-like structures with the extremities of the legs linked together.

1.1.2 Boundary conditions

On the bidimensional simple gate structure, boundary conditions are applied on the two extremities. In particular they are a joint and a cart. On the tridimensional structure, boundary conditions are applied to the four angles of the structure from the top view perspective, two joints and two carts in such a way that only the first and last ribs are constrained while the ones in between are free to move. Boundary conditions are always applied on the extremities end surface, either in the bidimensional and tridimensional structures, with particular focus on the tridimensional one, due to the configurations admitting either up and down facing extremities.

1.2 Free vibration analysis

The purpose of this analysis is unveiling the vibrational modes of the various bidimensional structures in order to identify the optimal gate discretization to be used in the upcoming tridimensional analysis. In addition shear locking with Mixed Interpolation Tensorial Components (MITC) algorithm is added to some bidimensional configurations in order to explore the influence of the phenomenon on the modal analysis.

1.2.1 Gate frequencies deviation

The major topic of interest is the comparison between the various gate models tested with the aid of some graphics. Figure 1.3 summarizes the first six modes and compares them to the most complex model taken into consideration (24L16). On the horizontal axis is highlighted the computational weight of the various solutions with respect to the reference and on the vertical axis a logarithmic scale allows to appreciate the variation from the reference modes. Also a yellow horizontal line marks the two percent variation to provide a better view of the goodness of the models plotted. Full results of the analysis is presented in Table 1.1 on page 25.

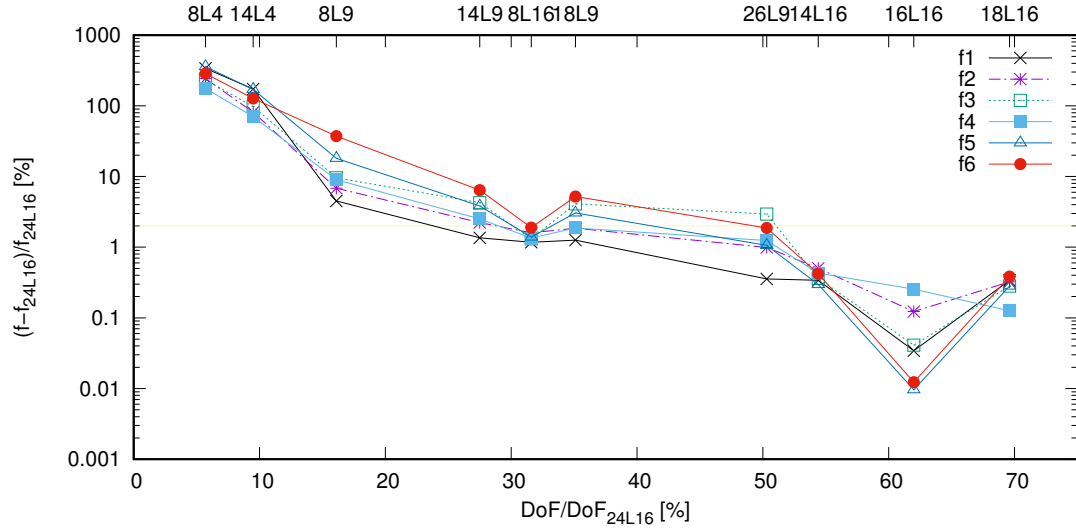


Figure 1.3: Frequencies deviation from reference (24L16)

LE efficiency

From the Figure 1.3 it can be seen a notable difference from the different type of LE discretization applied to every configurations, with the LE4 cells unable to provide reasonable results with every given distributions. Also LE9 cells seem to be quite unfitted to provide low error, as well the most refined distributions, also a high variations between the modes in the configuration itself is seen. Instead, LE16 cells appear quite precise even considering unrefined distributions. Taking into account the distribution, the difference between the 14 and the 18 element configurations are almost absent and all the frequencies variation for the 16 element gate are below the one percent even considering the high spread, with a 38% saving in the computational cost. This last configuration (16L16), designed to simplify construction of the tridimensional ribs, is fully validated and able to compete with the originally chosen configuration (14L16) with only a six percent increase in computational cost.

1.2.2 Shear locking

Shear locking is a phenomenon that occurs in finite element analysis with low thicknesses due to an overstating of the shear stiffness of the structure. This

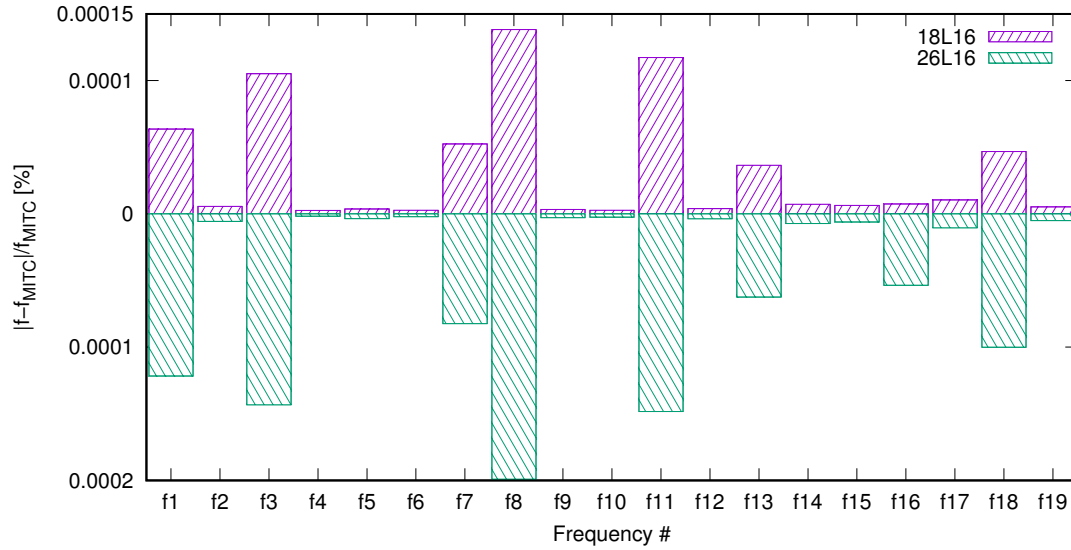


Figure 1.4: Frequencies variation with shear locking compensating algorithm

phenomenon can be mitigated with algorithms like the MITC used for the analysis presented in this report. Figure 1.4 is used to compare the two relevant applications of the shear locking correcting algorithm. The horizontal axis displays all the 20 modes computed and the vertical axis the variation between the frequency with and without the MITC algorithm.

Table 1.1 contains also the results for the 8L4 configuration, but the variations are too marginal to be significant in this study.

Shear locking impact

For each of the configurations taken into consideration in this graph the variation between the analysis with or without the MITC algorithm is small, almost unnoticeable, with few peaks for almost the same frequencies, except for the 16th frequency where the contribute of the MITC algorithm is more noticeable in one configuration (26L16) than the others. Also, this configuration experiences more variations on average. These information may suggest a rise in the importance of the mitigation effect of the algorithm with the increase of the number of elements in the configuration. Further analysis may reveal a stronger importance in case of stacked gate-like geometries.

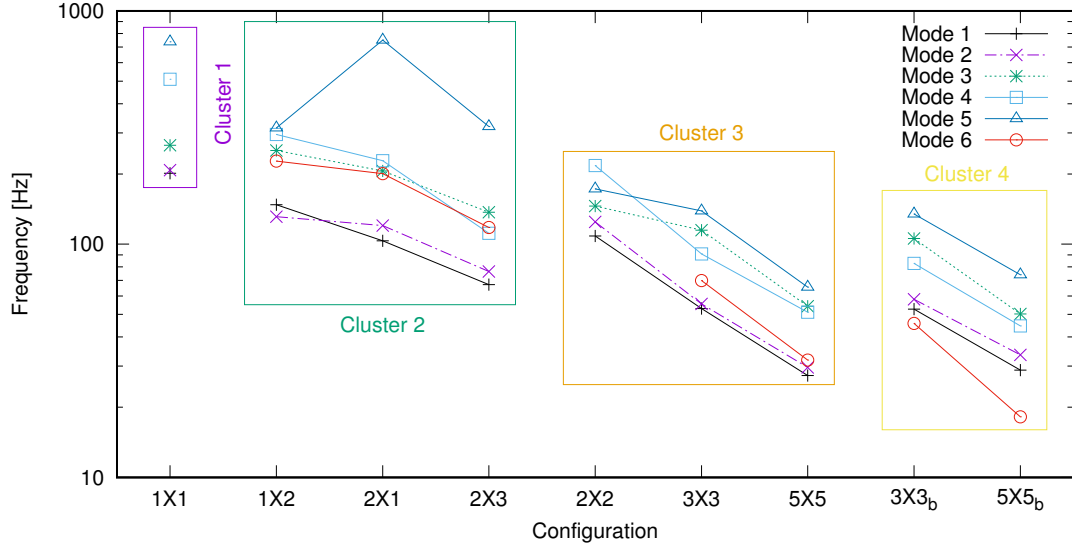


Figure 1.5: Frequencies for the various configurations

1.2.3 3D structure frequencies analysis

The purpose of the tridimensional modal analysis is to identify the most practical configuration for the material characterization from the two options described on the previous section. Figure 1.5 summarize the results from the first six mode for various planar extension ($N \times N$) and configuration ($N \times N_b$).

Modes analysis

Initially six modes are identified and described in the Table 1.2 on page 26. First five modes are specific of the 1X1 structure that is the foundation for further extension, sixth mode is unique of extended structure and it is absent on the 1X1 structure.

Graph in Figure 1.5 is divided in multiple cluster depending on the geometry of the structure. First cluster contains only the simplest structure result as reference for other structures. Second cluster contains irregular structures: indeed, it should be noted that the ones with odd depth dimension have much higher mode frequency that decay with increasing dimension. Third cluster contains regular structures: here it can be seen a general reduction of the frequencies in the

same mode with increase of dimensions. Last cluster includes the two symmetrical structures analysed: a decreasing trend can be observed here too, with higher frequencies on average relative to the previous cluster.

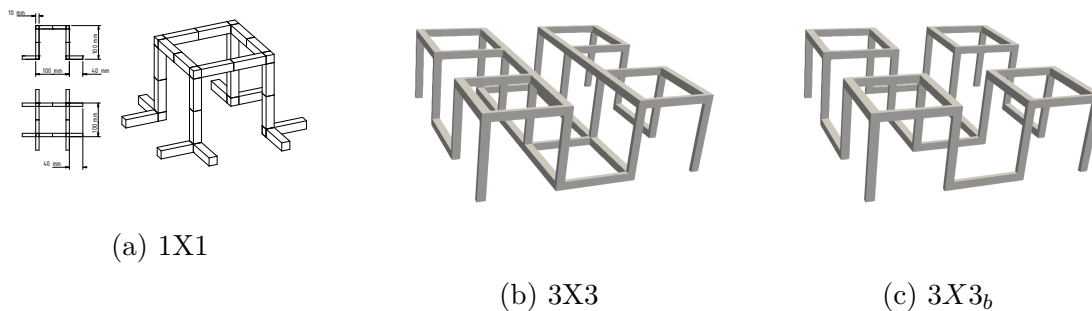


Figure 1.6: 3X3 configurations

1.2.4 Configurations analysis

Configuration in Figure 1.6c is made removing the spars that connect the angles of the gates, this configuration allows a symmetry on the expansion plane (xy). Instead, classical configuration, as seen in Figure 1.6b, is not symmetrical on the plane. In particular cluster three and four from Figure 1.5 are relevant to this analysis. From these clusters a similar performance can be seen for singular modes (1 to 5) with a noticeable reduction in frequencies for the sixth mode to appear. Also a lower decrease of frequency is linked to the expansion of the geometry (from 3X3 to 5X5) especially for the first five modes.

One more configuration involves the addition of more beams on the free ends of the structure. The resulted 'c' configuration may be the target for more analysis.

Freq	<i>Configurations</i>										<i>MITC</i>			
	8L4	14L4	8L9	14L9	8L16	18L9	26L9	14L16	16L16	18L16	26L16	8L4M	18L16M	26L16M
f1	705.1	437.8	167.8	162.7	162.4	162.6	161.1	161.1	160.5	161.1	160.5	705.1	161.1	160.5
f2	887.9	469.4	276.6	264.8	263.1	263.8	261.6	260.3	259.3	259.8	259.0	887.9	259.8	259.0
f3	1241.4	733.4	407.1	387.5	376.5	386.8	382.5	373.0	371.8	372.7	371.6	1241.4	372.7	371.6
f4	2340.6	1445.0	925.2	869.9	860.1	864.5	859.2	852.3	850.8	849.7	848.6	2340.6	849.7	848.6
f5	5214.1	3077.2	1339.0	1177.4	1149.8	1168.6	1146.1	1137.4	1133.9	1137.3	1134.1	5214.1	1137.3	1134.1
f6	6275.5	3696.0	2236.4	1732.8	1659.1	1713.1	1658.8	1635.2	1628.5	1634.6	1628.3	6275.5	1634.6	1628.3
f7	7359.7	4473.2	2257.4	1887.7	1830.8	1871.8	1836.5	1818.1	1814.0	1817.9	1814.0	7359.7	1817.9	1814.0
f8	8651.9	4994.4	2460.0	2259.3	2233.8	2246.6	2229.4	2215.7	2211.8	2212.6	2209.3	8651.9	2212.6	2209.3
f9	9095.9	5621.5	4390.9	3541.0	3457.3	3492.9	3434.6	3389.9	3375.6	3377.1	3365.3	9095.9	3377.1	3365.3
f10	9076.1	6918.9	4487.3	3935.8	3894.2	3897.9	3743.3	3706.7	3698.4	3704.0	3695.4	9076.1	3704.0	3695.4
f11	10466.8	7482.5	5423.9	4334.3	4235.2	4313.5	4012.0	3978.5	3960.7	3975.2	3957.4	10466.8	3975.2	3957.4
f12	11055.7	8421.8	6614.6	4438.4	4344.8	4371.7	4320.1	4270.9	4265.3	4256.6	4252.9	11055.7	4256.6	4252.9
f13	13132.8	8618.7	7672.6	5173.3	5134.0	5098.6	4772.2	4704.5	4687.9	4702.8	4683.9	13132.8	4702.8	4683.9
f14	11671.7	9086.2	8248.2	6252.2	6227.6	6220.6	6173.1	6144.2	6136.8	6137.9	6131.2	11671.7	6137.9	6131.2
f15	11642.9	9460.6	8371.2	6939.9	6638.0	6872.1	6720.9	6532.1	6520.5	6518.0	6506.3	11642.9	6518.0	6506.3
f16	17797.1	11816.3	8554.1	7528.8	7502.2	7478.5	7029.6	6847.2	6820.0	6831.5	6798.2	17797.1	6831.5	6798.2
f17	25250.0	13108.0	9110.6	7741.7	7575.6	7516.4	7446.5	7425.1	7406.8	7423.8	7406.7	25250.0	7423.8	7406.7
f18	26582.6	14572.2	9952.3	8190.7	7869.0	8020.7	7895.3	7559.9	7537.6	7545.0	7522.6	26582.6	7545.0	7522.6
f19	29365.0	14783.4	10357.0	8235.0	8192.6	8168.0	7947.8	7866.6	7840.8	7855.7	7832.5	29365.0	7855.7	7832.5
f20	31042.3	15564.4	12770.8	9400.7	9289.9	9306.5	8426.1	8286.7	8235.6	8262.6	8203.1	31042.3	8262.6	8203.1
DoF	216	360	612	1044	1200	1332	1908	2064	2352	2640	3792	216	2640	3792

Table 1.1: Gate analysis results table [Hz]

Configuration	1X1	1X2	2X1	2X3	2X2	3X3	5X5	3X3_b	5X5_b
Mode 1 Lateral vibration with joint-mounted extremities deformation	201.3	147.5	103.4	67.1	108.4	52.9	27.3	52.7	28.8
Mode 2 Fixed bonds vibration along the depth	207.6	131.2	120.2	76.3	124.7	55.4	29.6	58.1	33.5
Mode 3 Head twist	265.6	252.2	206.1	137.1	145.7	114.9	54.2	105.7	50.3
Mode 4 Free extremities twist	509.5	295.4	228.2	111.4	217.3	90.8	51.1	82.7	44.6
Mode 5 Lateral vibration with carriage-mounted extremities deformation	737.7	315.1	750.6	319.4	-	138.9	65.4	134.7	73.9
Mode 6 Out of plane vibration	-	226.9	200.7	117.8	172.7	69.9	31.9	45.7	18.2

Table 1.2: Tridimensional structure modes

Chapter 2

Material characterization

2.1 Introduction

For the previous simulation the material used was always an aluminium alloy (AlAll) with the properties shown in the Table 2.1. In this chapter, instead, the materials combination and distribution will be addressed. This topic is relevant in order to evaluate the effect of the strength and density distribution among the structure on the vibrational analysis. Firstly the choice of materials and their combination will be covered, then a brief analysis of the variation generated by the material change will lead to the selection of the most relevant materials combination to finally perform a distribution analysis.

Material	E [GPa]	ν [-]	ρ [kg/m ³]	Description
Al2O3	340	0.22	3900	Alluminum oxide
AlAll	75	0.33	2700	Generic Al alloy
CoCrMo	240	0.35	8250	Chrome alloy
SS316	193	0.33	8000	Stainless steel
Ti6Al4V	114	0.33	4430	Titanium alloy
TiC	450	0.19	4940	Titanium ceramic

Table 2.1: Materials used in the study

2.2 Materials selection

The choice of materials to include in the study is made bearing in mind the current production capabilities for multimaterial parts. The most relevant production technology in this field lies in the Addictive Manufacturing (AM), especially the techniques for metal AM with stream of material in forms of wires or powder. Suitable AM techniques are summarised on Table 2.2. The most notable process is the Laser Engineering Net Shaping (LENS) that uses a laser to create a weld pool where the powdered metal is deposited through a specialized nozzle [1].

Meanwhile metal-ceramic multimaterial structures have yet to enter the mature stage due to the large discrepancies in the thermal properties that may cause the vaporisation of the metallic material during the fusion of the ceramic one. However some metal-ceramics combinations have been tested with bright results and a ceramic coated material is easy to obtain even with current technologies. Besides AM, traditional manufacturing processes can be used to produce mixed materials structure by introducing an assembly step down the line in order to join the various structure created with each material.[2]

Technique	
DMLF	Direct Metal Laser Fusion
EBAM	Electron Beam AM
DMD	Direct Metal Deposition
LENS	Laser Engineering Net Shaping
LMWD	Laser-based Metal Wire Deposition
HAM	Hybrid AM

Table 2.2: Addictive Manufacturing metal technique

2.2.1 Combination

Besides the material choice, the combinations between the selected ones is equally or even more important than the early selection. The permutation selected for the analysis are summarised in Table 2.3, where the first two rows identify the single material structures, while the following rows contain the multimaterial ones. The

materials combinations are selected keeping in mind the compatibility between materials and the manufacturing capabilities needed. The most notable combination is the ones between Stainless Steel (SS316) e Alumina (Al₂O₃). Besides what already written for the combination of metals and ceramics, this combination has been proven successful through LENS technique [4].

Material 1		Material 2	$\frac{E_1}{E_2}$	$\frac{\rho_2}{\rho_1}$	$\frac{\nu_1}{\nu_2}$
AlAll	+	AlAll	1		1
SS316	+	SS316	1		1
SS316	+	Al ₂ O ₃	0.276		1.5
Ti6Al4V	+	TiC	0.227		0.3
SS316	+	Ti6Al4V	0.937		0.9
Ti6Al4V	+	CoCrMo	0.884		0.9

Table 2.3: Materials combination

2.3 Simulation

For the next simulations an improved model will be used. In particular, lower beams originated from the legs have been added to enhance simmetry and to ease the future application of periodic boundary conditions on the geometry. For the first batch of simulations, various combinations are tested, beams are added only on the x direction; for the second batch, where various distributions are tested, beams are also added on the y direction. Moreover, only 2X2 and 4X4 configurations will be analysed on this chapter: this choice is made in order to focus on how the material properties could impact on the performance of the structure rather than the geometry used for the structures.

2.3.1 Materials selection

The choice for the materials to be used in the next section is made by comparing 2X2 and 4X4 structures made by the materials combinations in Table 2.3. Each combination is applied on both the geometries by placing the first material on the ribs (blue) and the second on the spars (green) as rapresented on Figure 2.1.

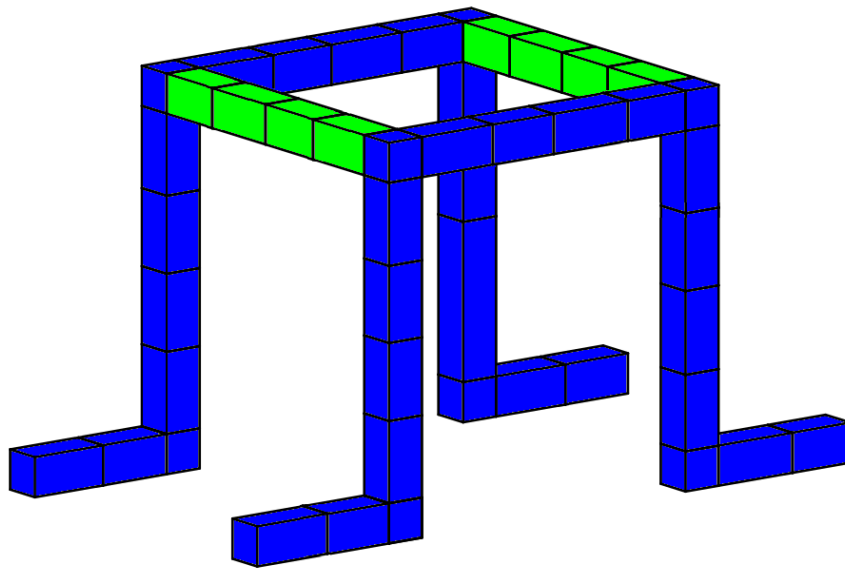


Figure 2.1: 1X1 configuration with highlighted ribs (blue) and spars (green)

Then the geometry is supplied to the Mul2 software for the modal analysis, results are collected and analysed with a Modal Assurance Criterion (MAC) matrix and the first six modes are considered. For each mode, resulting frequencies are fitted on a plane on the ratio between the specific Young's module and the Poisson's numbers of the combinations. The choice of fitting the results to a plane is made in order to offer an elementary prediction on the effect to be expected by changing the materials properties. These results are represented in Figure 2.2. Those graphs highlight a consistent higher value on the top left with low specific Young's module ratio and high Poisson's number ratio. Consequently the most suitable combination taken into consideration during the analysis is SS316 + Al2O3.

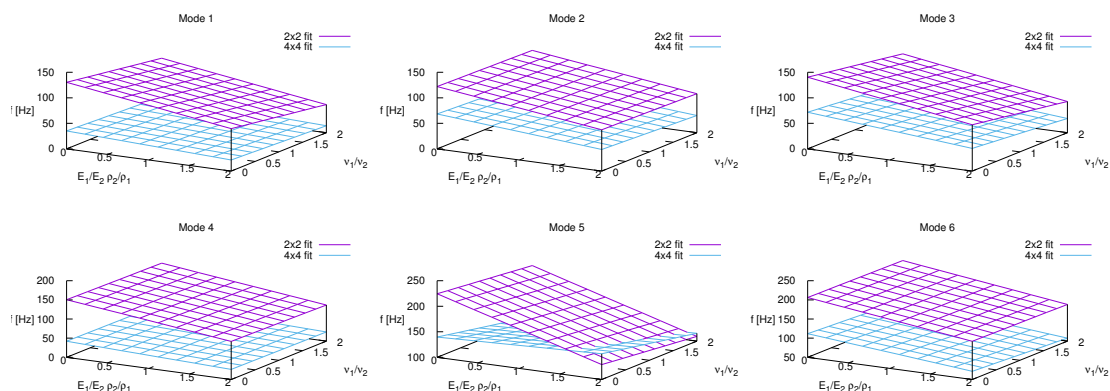


Figure 2.2: Fitted result of the analysis on materials combinations

2.3.2 Materials distribution

The second batch of simulations, done with combination SS316 + Al2O3, is focused on how the distribution of materials can affect the modal properties of the structure. Four distributions are proposed with one more for comparison. This last distribution is randomised to blend most of the discontinuity while maintaining approximately the same density as the four proper distributions. Those are identified by a sequential lettering, from *a* to *d*, and they are represented in Figure 2.3. For each of them, a description is provided below:

- a.* This configuration is the same as the one used in the materials combinations

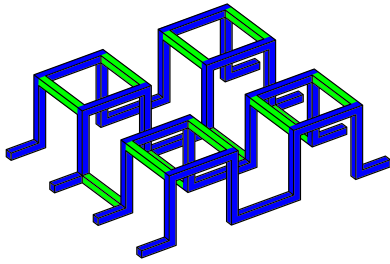
analysis, with the ribs (4) made of SS316 steel and the spar (5) made of aluminium oxide.

- b.* This configuration is made by alternating materials on the y direction in a way that each 1X1 geometry is split in the middle, so each adjacent *half spar-rib-half spar* unit has a different material.
- c.* This configuration is similar to the previous one, but with the entire 1X1 geometry made of the same material. In this case the 2X2 geometry used for the analysis is split in half on the y direction.
- d.* The last configuration is made in order to obtain an intended result, at least elementary. In contrast with the previous ones, this configuration develops on the z direction. The bottom and top layers are made of the stiffer material, in this case alumina, while the steel, that is more elastic, is applied on the middle beams.

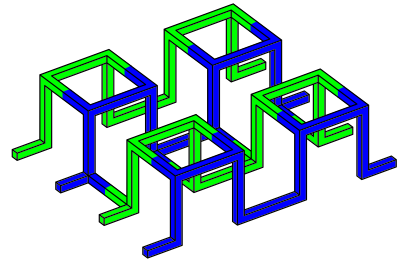
The configurations are then loaded on the Mul2 software to execute a modal analysis and the data, in form of modal frequencies and displacement, are extracted and analysed. Firstly every distribution mode is classified with a MAC matrix, then the frequencies are plotted as a ratio between the configuration frequency and the base (randomized) frequencies of the same mode. The result of the analysis is presented in Figure 2.4.

Distributions results

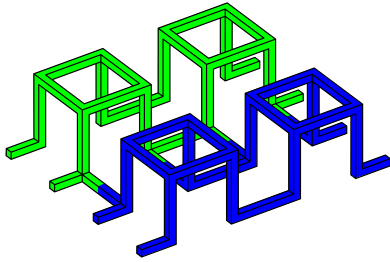
On Figure 2.4 the first six modes frequencies are represented with respect to the base distribution. From this graph vertical axis extension is clear that the difference between the configurations rarely exceeds 15% with the exception of configuration *c* that shows a bigger variation, especially on the fourth and sixth modes. This behaviour may be linked more to the mass distribution than to the materials properties, indeed most of the weight is located in the more dense half of the geometry, where the material is alumina. Configuration *a* and *b* are similar with the second one slightly more wide. Finally, configuration *d* may be the only one where the materials distribution affects the results, with all the modal frequencies 10% to 15% higher than the randomized distribution ones.



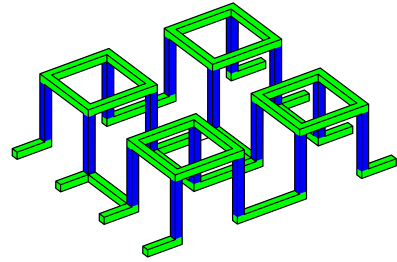
(a) Configuration *a*.



(b) Configuration *b*.



(c) Configuration *c*.



(d) Configuration *d*.

Figure 2.3: 2X2 configurations

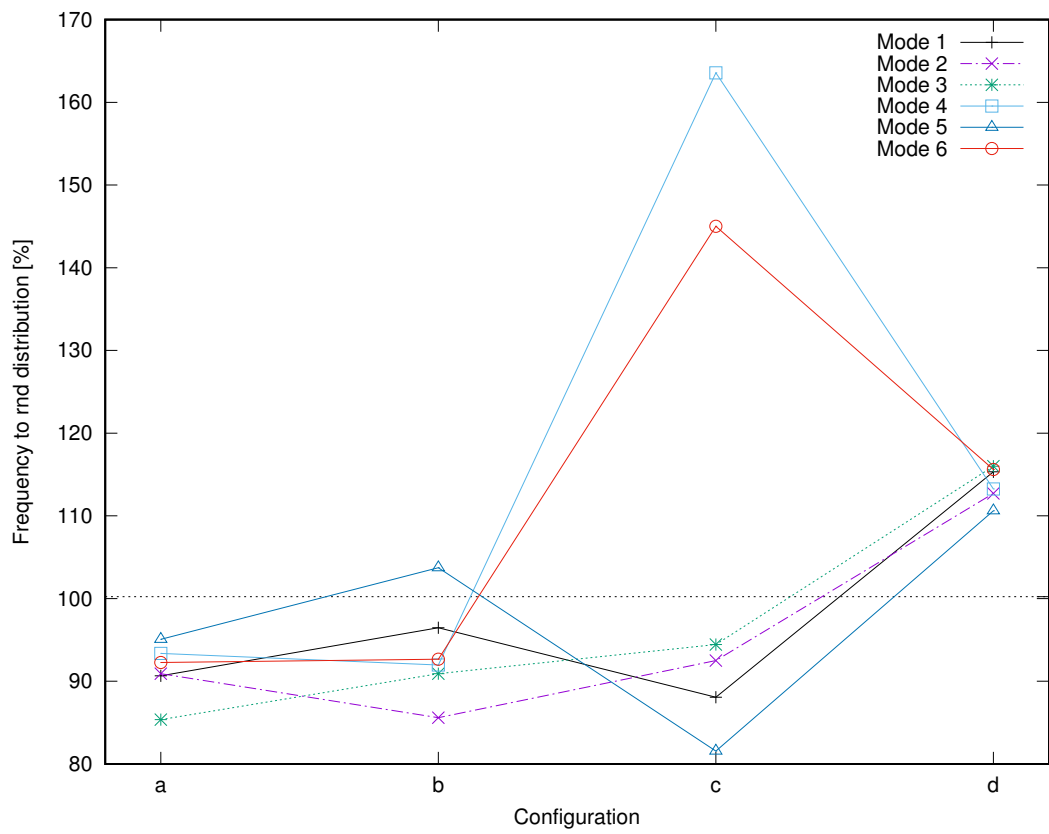


Figure 2.4: Frequency variation for the first six modes

Part II

Wave analysis

Chapter 3

Wave propagation problem

3.1 Introduction

The purpose for this chapter is the implementation of a wave propagation problem to probe the energy transfer mechanism in a waveguide, to which many structural components can be referred. This analysis can lead to a better understanding of the acoustic emissions and vibration of the structure to conceive strategies to manipulate them. Analytical or exact solutions are available for simple structures, while complex structures require extensive analysis with semi-analytical or numerical techniques. The Wave Finite Element (WFE), the algorithm used in this chapter, is one of the most powerful techniques if used in conjunction with a solid FE theory, that in this case is the CUF. This technique uses the matrices computed for a section of the waveguide via an FE package to propagate the structure in one or more directions and solve the wave propagation problem [6].

Theories

Various theories can be used to solve the wave propagation problem of the structure, that is the subject of this document.

The first method to be discussed is the **Dynamic Stiffness Method (DSM)**. In this method the structure is divided into simple elements with the Degree of Freedom defined on different nodes, and a dynamic stiffness matrix D is established in the frequency domain to relate nodal responses to forces. To obtain this

matrix, the analytical solutions of the element governing differential equations, for harmonically varying displacements, are calculated and then assembled as in standard FEM. This method can be considered as exact and it has already been used for study of helical spring and aircraft panels.

The **Spectral Element Method (SEM)** target is still to assemble the dynamic stiffness matrix, but this time the matrix is formulated in the frequency domain from the general solution of the equation of motion represented by a spectral form. The solution is assumed to be a sum of simple harmonic waves at different frequencies and so the solution can be reconstructed in the time domain with a Fast Fourier Transform. This method can be applied to one-dimensional waveguides while the development of the spectral elements becomes difficult for two-dimensional application.

The **Transfer Matrix Method (TMM)** rely on the division of the structure, usually a plate, into layers and then on assembling the layer transfer matrix and global transfer matrix with elements from each layers. This method is able to calculate the exact solution of a multilayer plate with arbitrary stacking sequence. It can be also applied to periodic structures by combining the states of the left hand of the first period structure with the right hand of the next period structure via a transfer matrix.

The **Thin Layer Method (TLM)** combines the finite element method in the direction of the cross section with the analytical solution in the form of wave propagation in the remaining directions. This method was proved effective on laminated plates with viscoelastic layers where each lamina is divided into homogeneous sub-layers.

The **Spectral Finite Element Method (SFEM)** is mostly used with one-dimensional wavelines. It uses the same concept of the TLM but with inverted cross sections and length discretisations. In particular, this method uses FE discretisation for the cross section instead of the length discretisation in order to evaluate short wavelength propagation on the waveguide. This method requires complex formulation for new spectral elements and coupling operators.

The **Receptance Method (RM)** uses the reciprocal of the dynamic stiffness matrix, i.e. receptance matrix, to relate the states of the left and right hand of the periodic element.

3.1.1 WFE Theory

The power of the WFE method lies in the capability to expand the problem on the second dimension, enabling the capability to analyse tridimensional structures with homogeneity along two different directions. Another relevant characteristic is the reduction of the vibrational problem to a more suitable eigenproblem. Also, the use of matrices obtainable from common FE packages made the method easy to use in a great number of structures without the needs to reform the procedure for every structure.

The WFEM process start with the modelling of the first period of the structure and the creation of the mesh to be used for the FEA. Then the structure is analysed with a FE package, in this case the CUF one, where the structural matrix \mathbf{C} and mass matrix \mathbf{M} are produced. Once the structural matrices have been obtained from the CUF package, the dynamic stiffness matrix \mathbf{D} can be assembled and successively decomposed in order to isolate the left (L) and right (R) cross sections and the internals (I) nodes.

$$(\mathbf{K} + j\omega\mathbf{C} - j\omega^2\mathbf{M})\mathbf{q} = \mathbf{f} \quad \mathbf{D}(\omega)\mathbf{q} = f \quad (3.1)$$

In the absence of internal forces, $\mathbf{f}_I = 0$, the internal displacements \mathbf{q}_I can be extracted as a function of the left and right cross section displacements and a reduced matrix can be assembled as in Equation 3.6.

$$\begin{pmatrix} \tilde{\mathbf{D}}_{LL} & \tilde{\mathbf{D}}_{LI} & \tilde{\mathbf{D}}_{LR} \\ \tilde{\mathbf{D}}_{IL} & \tilde{\mathbf{D}}_{II} & \tilde{\mathbf{D}}_{IR} \\ \tilde{\mathbf{D}}_{RL} & \tilde{\mathbf{D}}_{RI} & \tilde{\mathbf{D}}_{RR} \end{pmatrix} \begin{pmatrix} \mathbf{q}_L \\ \mathbf{q}_I \\ \mathbf{q}_R \end{pmatrix} = \begin{pmatrix} \mathbf{f}_L \\ \mathbf{f}_I \\ \mathbf{f}_R \end{pmatrix} \quad (3.2)$$

$$\mathbf{q}_I = -\tilde{\mathbf{D}}_{II}^{-1}(\tilde{\mathbf{D}}_{IL}\mathbf{q}_L + \tilde{\mathbf{D}}_{IR}\mathbf{q}_R) \quad (3.3)$$

$$\begin{aligned} \mathbf{D}_{LL} &= \tilde{\mathbf{D}}_{LL} - \tilde{\mathbf{D}}_{LI}\tilde{\mathbf{D}}_{II}^{-1}\tilde{\mathbf{D}}_{IL} \\ \mathbf{D}_{LR} &= \tilde{\mathbf{D}}_{LR} - \tilde{\mathbf{D}}_{LI}\tilde{\mathbf{D}}_{II}^{-1}\tilde{\mathbf{D}}_{IR} \\ \mathbf{D}_{RL} &= \tilde{\mathbf{D}}_{RL} - \tilde{\mathbf{D}}_{RI}\tilde{\mathbf{D}}_{II}^{-1}\tilde{\mathbf{D}}_{IL} \\ \mathbf{D}_{RR} &= \tilde{\mathbf{D}}_{RR} - \tilde{\mathbf{D}}_{RI}\tilde{\mathbf{D}}_{II}^{-1}\tilde{\mathbf{D}}_{IR} \end{aligned} \quad (3.4)$$

$$\mathbf{D}_{LL}^T = \mathbf{D}_{LL} \quad \mathbf{D}_{RR}^T = \mathbf{D}_{RR} \quad \mathbf{D}_{RL}^T = \mathbf{D}_{RL} \quad (3.5)$$

$$\begin{pmatrix} \mathbf{D}_{LL} & \mathbf{D}_{LR} \\ \mathbf{D}_{RL} & \mathbf{D}_{RR} \end{pmatrix} \begin{pmatrix} \mathbf{q}_L \\ \mathbf{q}_R \end{pmatrix} = \begin{pmatrix} \mathbf{f}_L \\ \mathbf{f}_R \end{pmatrix} \quad (3.6)$$

By indexing the succession of elementary sections by the letter s , so the following section is $s + 1$, the continuity between them can be written as in Equation 3.7 with the right cross section displacements equal to the right side of the next section and the sum of the forces on the cross sections equal to zero.

$$\begin{pmatrix} \mathbf{q}_L^{s+1} \\ \mathbf{f}_L^{s+1} \end{pmatrix} = \begin{pmatrix} \mathbf{q}_R^s \\ -\mathbf{f}_R^s \end{pmatrix} \quad (3.7)$$

From Equation 3.6 is possible to derive the transfer matrix between two consecutive left cross sections as in Equation 3.8.

$$\begin{pmatrix} \mathbf{q}_L^{s+1} \\ \mathbf{f}_L^{s+1} \end{pmatrix} = \mathbf{T} \begin{pmatrix} \mathbf{q}_L^s \\ \mathbf{f}_L^s \end{pmatrix} \quad \text{with} \quad \mathbf{T} = \begin{pmatrix} -\mathbf{D}_{LR}^{-1}\mathbf{D}_{LL} & \mathbf{D}_{LR}^{-1} \\ -\mathbf{D}_{RL} + \mathbf{D}_{RR}\mathbf{D}_{LR}^{-1}\mathbf{D}_{LL} & -\mathbf{D}_{RR}\mathbf{D}_{LR}^{-1} \end{pmatrix} \quad (3.8)$$

For a free wave propagating through a waveguide, the displacements and forces at successive cross sections can be also represented as in Equation 3.9. With Equations 3.7, 3.8 and 3.9 the eigenproblem can finally be made explicit in Equation 3.11.

$$\begin{pmatrix} \mathbf{q}_R \\ \mathbf{f}_R \end{pmatrix} = \lambda_y \begin{pmatrix} \mathbf{q}_L \\ \mathbf{f}_L \end{pmatrix} \quad \text{with} \quad \lambda_y = e^{-jk\Delta} \quad (3.9)$$

$$\begin{pmatrix} \mathbf{q}_L^{s+1} \\ \mathbf{f}_L^{s+1} \end{pmatrix} = \lambda_y \begin{pmatrix} \mathbf{q}_L^s \\ \mathbf{f}_L^s \end{pmatrix} \quad (3.10)$$

$$\mathbf{T} \begin{pmatrix} \mathbf{q}_L^s \\ \mathbf{f}_L^s \end{pmatrix} = \lambda_y \begin{pmatrix} \mathbf{q}_L^s \\ \mathbf{f}_L^s \end{pmatrix} \quad (3.11)$$

$$\begin{aligned}
\begin{pmatrix} \mathbf{q}_L \\ \mathbf{q}_I \\ \mathbf{q}_R \end{pmatrix} &= \mathbf{\Lambda}_R \begin{pmatrix} \mathbf{q}_L \\ \mathbf{q}_R \end{pmatrix} & \begin{pmatrix} \mathbf{f}_L \\ \mathbf{f}_I \\ \mathbf{f}_R \end{pmatrix} &= \mathbf{\Lambda}_L \begin{pmatrix} \mathbf{f}_L \\ \mathbf{f}_R \end{pmatrix} \\
\mathbf{\Lambda}_R &= \begin{pmatrix} \mathbf{I} & 0 \\ 0 & \mathbf{I} \\ \lambda_y \mathbf{I} & 0 \end{pmatrix} & \mathbf{\Lambda}_L &= \begin{pmatrix} \mathbf{I} & 0 & 0 \\ 0 & \mathbf{I} & \lambda_y^{-1} \mathbf{I} \end{pmatrix}
\end{aligned} \tag{3.12}$$

$$(\mathbf{\Lambda}_L \mathbf{K} \mathbf{\Lambda}_R + j\omega \mathbf{\Lambda}_L \mathbf{C} \mathbf{\Lambda}_R - \omega^2 \mathbf{\Lambda}_L \mathbf{M} \mathbf{\Lambda}_R) \bar{\mathbf{q}} = 0 \tag{3.13}$$

The i -th eigenvalue can be written as $\lambda_i = e^{-i\kappa_j \Delta} = e^{-\mu_i \Delta} e^{-j\kappa_i' \Delta}$ where the complex wavenumber $\kappa_i = \kappa_i' - j\mu_i$ is decomposed into its real (κ_i') and imaginary (μ_i) parts which are equal, respectively, to the attenuation and phase change per unit length of the i -th wave. The direction and type of wave can be inferred from the nature of the eigenvalue and the two parts that compose it. Different types of waves are summarised on Table 3.1.

Direction	Wave	λ	$ \lambda $	μ	κ'
Positive	propagating	imaginary	1	0	> 0
	evanescent	real	< 1	> 0	0
	attenuating	complex	< 1	> 0	> 0
Negative	propagating	imaginary	1	0	< 0
	evanescent	real	> 1	< 0	0
	attenuating	complex	> 1	< 0	< 0

Table 3.1: Eigenvalue properties and associated wave

3.1.2 Case studies

The purpose of this preliminary section is to explore the performance of various structures while introducing different types of alterations, both geometric and materials related. This goal is reached by analysing already published papers or thesis on WFEM analysis and changing the structures on those documents to reach a better understanding of the effect of those variations on the performance of the objects.

Simple cube tessellated beam

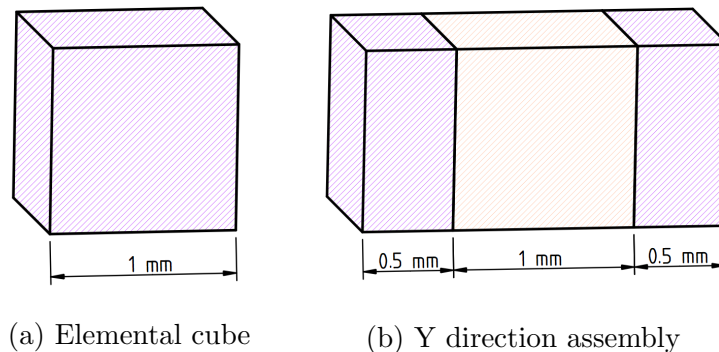


Figure 3.1: Models used in this analysis

The goal of this section is to analyse a simple beam structure taken from the thesis [5]. This beam is made by the recurrence of a simple cube with a 1 mm edge on the y direction as in Figure 3.1a. During the first batch of simulations this cube is made of steel, while in the second batch a multimaterials option is tested by dividing the cube along the z direction with the halves respectively made of steel and aluminium as in Figure 3.1b. Furthermore the two batches are exploited to verify various discretisation with the output known from the original document. This final batch also contains a full spectrum analysis of a proposed configuration with alternating cubes of steel and aluminium.

For all the figures below the procedure is the same: firstly the input files are compiled and processed by the CUF package, the stiffness and mass matrix are extracted and used by the WFEM code to generate the results that are then plotted for a better understanding and comparison. The first two figures hold the result from the first batch of simulation, that is the one with the single material cube and where the discretisation is tested on both the cross section expansion method and the finite element discretisation. The third figure holds the results from the multiple materials cube and here only the cross sectional expansion (Taylor or Lagrange) is analysed. The last one shows the full spectrum analysis.

By confronting the results obtained during the analysis with the results in the original document [5] the similarity between them is clear. Figure 3.2 shows perfectly where the points marked as *'thesis res'* are taken from the original doc-

ument. Focusing on our results, in this batch of simulations, permutations of two cross sectional Lagrange expansions (LE4 and LE9) and three depth beam discretisations (B2 to B4), with a total of six combinations, are tested. The most relevant ones are in the graph, in particular the most compute intensive LE9 - B4 and the two variations on the opposite end of the spectrum LE9 - **B2** and **LE4** - B4. The graph shows the propagation of three modes in the considered range: two with a constant velocity (b and c) and the third dampened (a). While in the last two there is no difference between the various discretisations, in the first (a) the transition from LE9 to LE4 causes a noticeable error in the results. The similarity between the B4 and B2 leads to a shift to the second discretisation for the second batch of simulations with multimaterials.

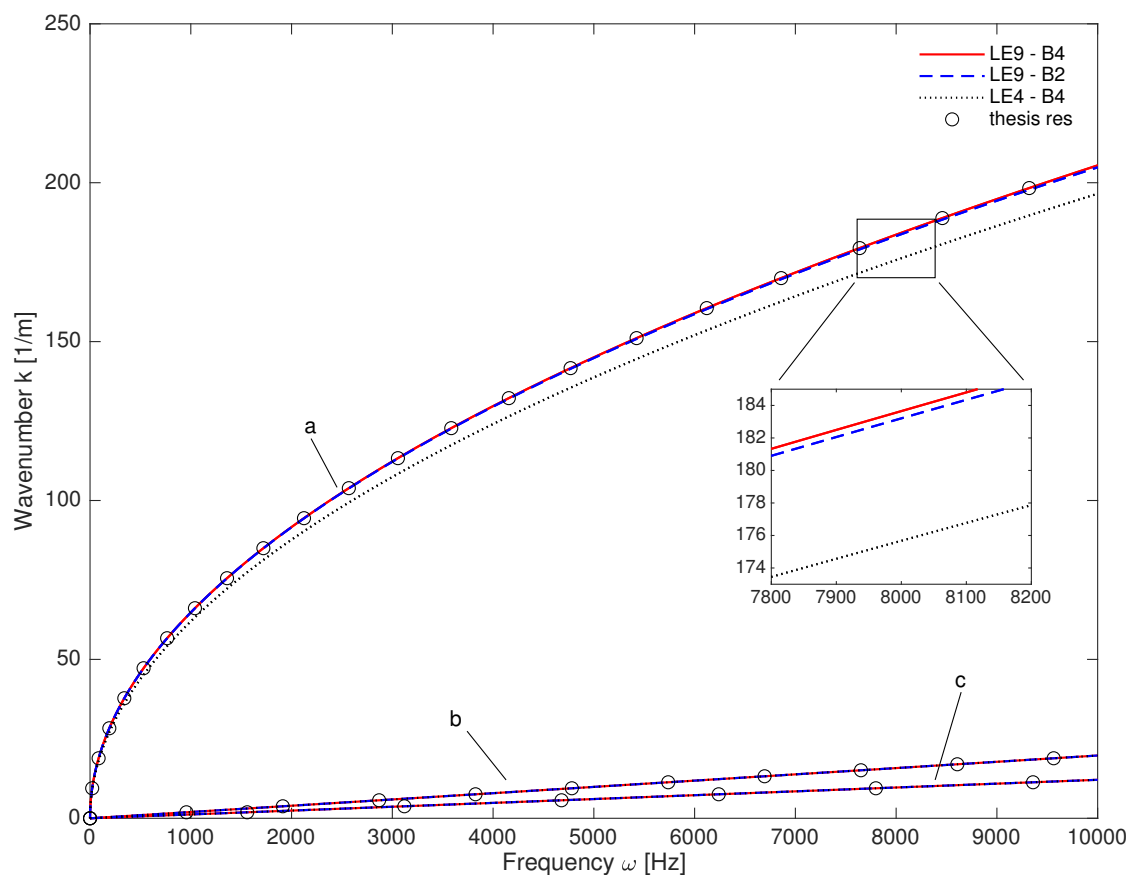


Figure 3.2: Single material cube with Lagrange expansions comparison

Figure 3.3 shows the result of the analysis on the single material cube discretised

with various orders of Taylor expansion on the cross section and the same as above in the FE nodes discretisation (B2, B3 and B4). In this case a bigger number of configurations are tested, with the expansion order range from the classical theories to an five-order Taylor expansion. In the graph only the most relevant configurations are proposed with the addition of the LE9 - B4 from the Lagrange analysis for reference. The TE-1 configuration uses the classical EBT model, while the TE0 represents the TBT model. TE1 is omitted since it is not different from the TE2 configuration and TE3 to TE5 show some type of instability. Also there is no difference from the B2 and B4 discretisations.

Reverting to the figure at hand, there is no error between the various expansion orders analysed, but the complete absence of the mode b from the classical theories expansion (TE-1 and TE0) suggests the use of at least the TE1 for the second batch of simulations.

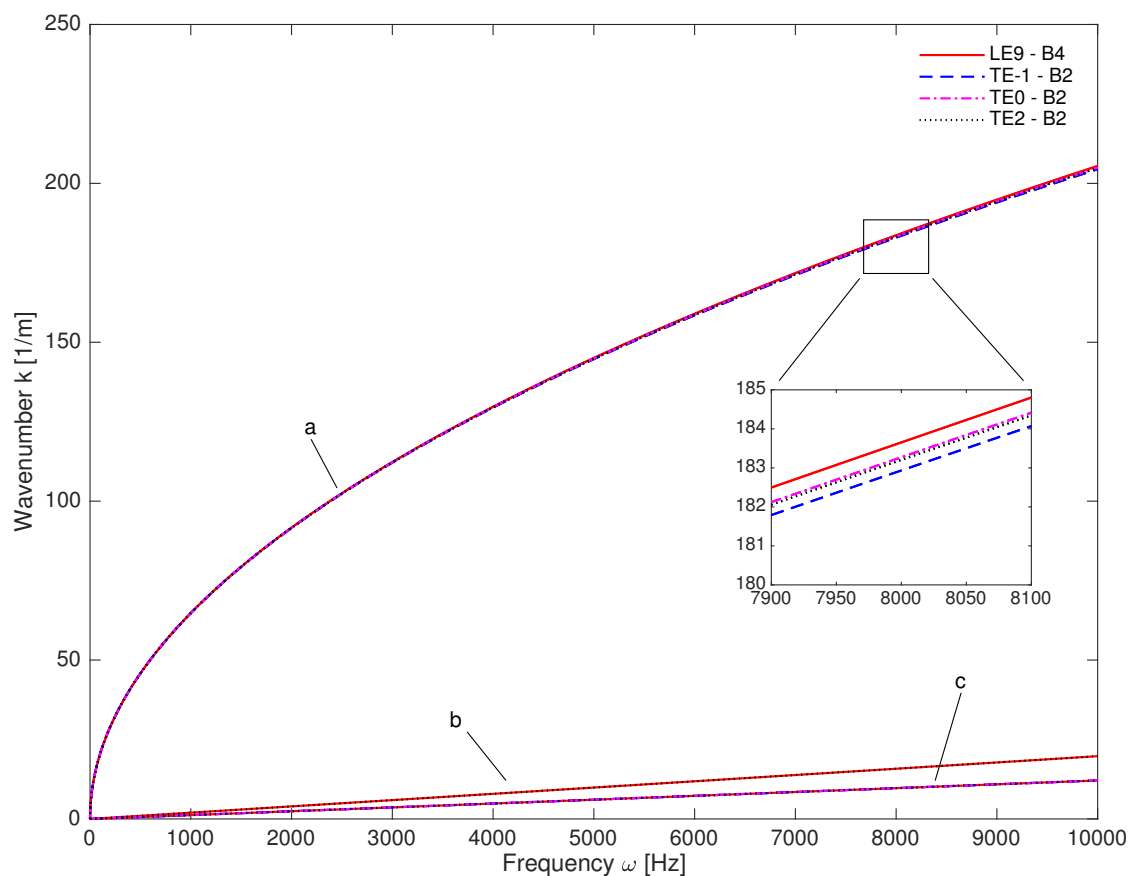


Figure 3.3: Single material cube with Taylor expansions comparison

Figure 3.4 is the first of the second batch of simulations, in which a multi-materials cube is taken into consideration with two different half splitting plane: z-x plane and y-x plane also referred respectively as y direction and z direction. On the coming figures the LE9 - B2, single material configuration is added for reference. In Figure 3.4 the results for the z direction splitting are shown and the first thing that become clear is the appearing of an extra mode, *d*. This fourth mode is displayed also on the single material analysis, but it is coincident with the *a* mode, so it is not identified in the first two figures. Besides the differentiation of the fourth mode, there is only one other difference between the Lagrange expansion case and the Taylor expansion one: the *c* mode is lightly shifted in the TE1 case than the reference and LE9 cases.

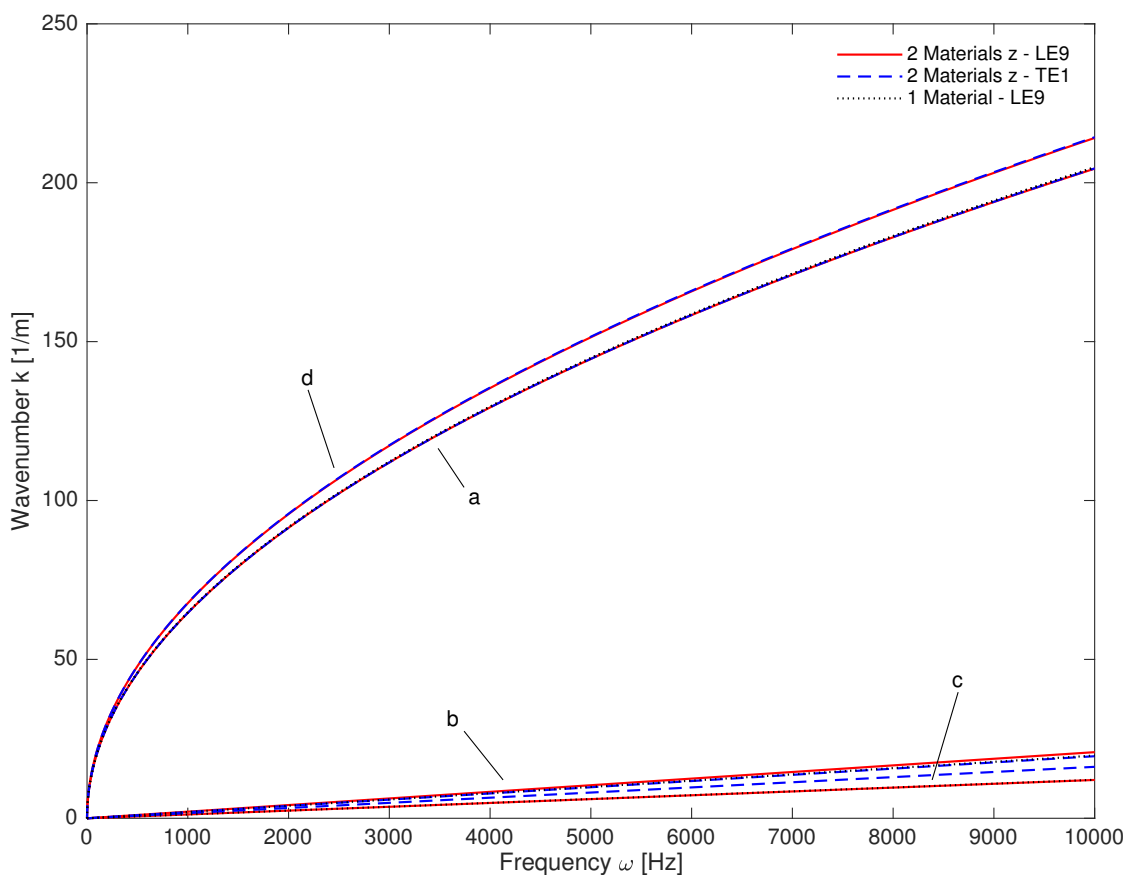


Figure 3.4: Multi material cube expansions method comparison

In the last analysis of the batch, full spectrum analysis of a different y config-

uration is analysed: this configuration is formed with a half cube of aluminium (blue), a full cube of steel (green) and another half cube of aluminium, as shown in Figure 3.1b. Figure 3.5 shows the presence of five stopbands with increasing width, the two most noticeable are between $1.63 \cdot 10^7 Hz$ and $1.77 \cdot 10^7 Hz$ and between $1.98 \cdot 10^7 Hz$ and $2.34 \cdot 10^7 Hz$.

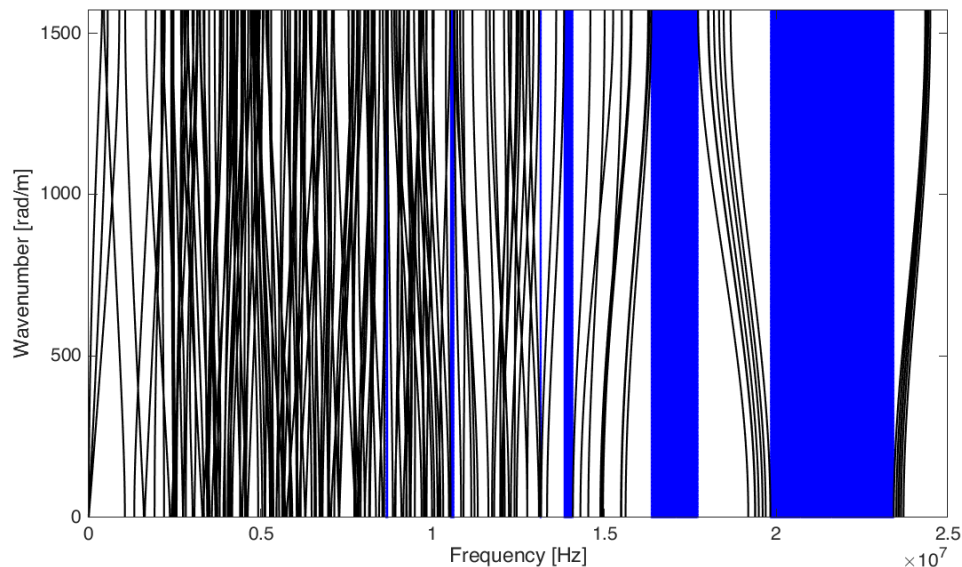


Figure 3.5: Spectrum analysis with stopband shown with a blue color

Periodic and quasi-periodic tessellated beams

In this section, the document [9] will be analysed with the intent of reaching a better understanding of how periodic and quasi-periodic base cells affect the performance of a tessellated beam and how the CUF code can maintain a high fidelity with respect to a more demanding solid simulation. In the base document two subcells, called A and B , are defined as shown in Figure 3.6. Each of them has a square cross-section but with different coupled dimensions as defined in Table 3.2. From those two subcells, two cells are assembled: one periodic with two subcells (AB), called Double Unit (DU), and the other one with 13 subcells in a manner (ABAABABAABAAB) defined by the 6th order Fibonacci sequence, called Super Unit (SU) and represented in Figure 3.7.

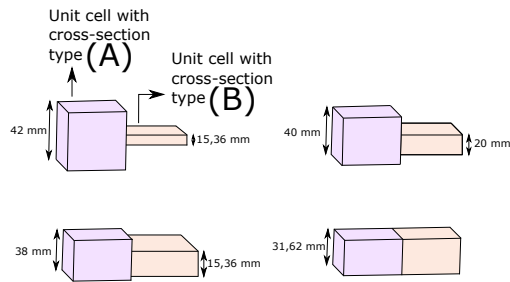


Figure 3.6: Duple Unit cell dimensions combination

Type	Cell	Width [mm]	Height [mm]	Ratio
I	A	42.00	42.00	2.7
	B	15.36	15.36	
II	A	40.00	40.00	2
	B	20.00	20.00	
III	A	38.00	38.00	1.6
	B	23.58	23.58	
IV	A	31.62	31.62	1
	B	31.62	31.62	

Table 3.2: Geometrical variation of the two subcells

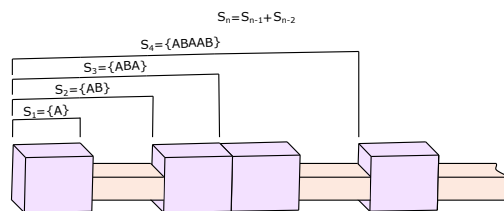


Figure 3.7: Super Unit cell Fibonacci sequence

For the CUF package elaboration, each subunit is modelled with a B4 beam with a second-order Taylor expansion on the cross-section and this discretisation can be seen in Figure 3.8. The reason for this choice is the result of a try and error process where firstly a Lagrange expansion with B2 was tested with poor results and both the cross-section and length discretisation bear issues for two different reasons: the Lagrange expansion for the cross-section causes the WFEM code to misinterpret the numbers of nodes in the cell left and right boundaries, which causes the \mathbf{D} to be badly assembled and the unreliable results; the choice of B2 discretisation for the length causes the flexional modes to be misrepresented and thus the results appear to be shifted to higher frequencies.

Both two subcells are made of Steel A-36.

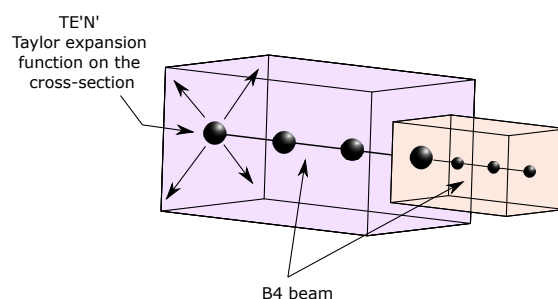


Figure 3.8: Double Unit cell discretization

In Figure 3.9 the results of the analysis of the Double Unit cell for each type are presented. The difference between the two models is almost invisible, indeed the results from the base document for this section (blue circles) are almost coincident with our result. Besides that, the shift in frequency of the bandgap is visible with the decrease of the ratio between the two subunit dimensions, from Type I bandgap around 750 Hz to Type III bandgap around 1500 Hz. Furthermore, the width of the bandgap increases with the decrease of the ratio. On the other hand, in the Type IV graph, the stopband disappears when there is no more difference between the two subcells dimensions.

In Figure 3.10 the results of the analysis of the Super Unit cell for each type are presented. In this case, even the difference between the two models is nearly invisible. The deviation is appearing only on the high frequencies, over 600 Hz. For Types I to III, three peaks with two stopbands are depicted in Figure 3.10

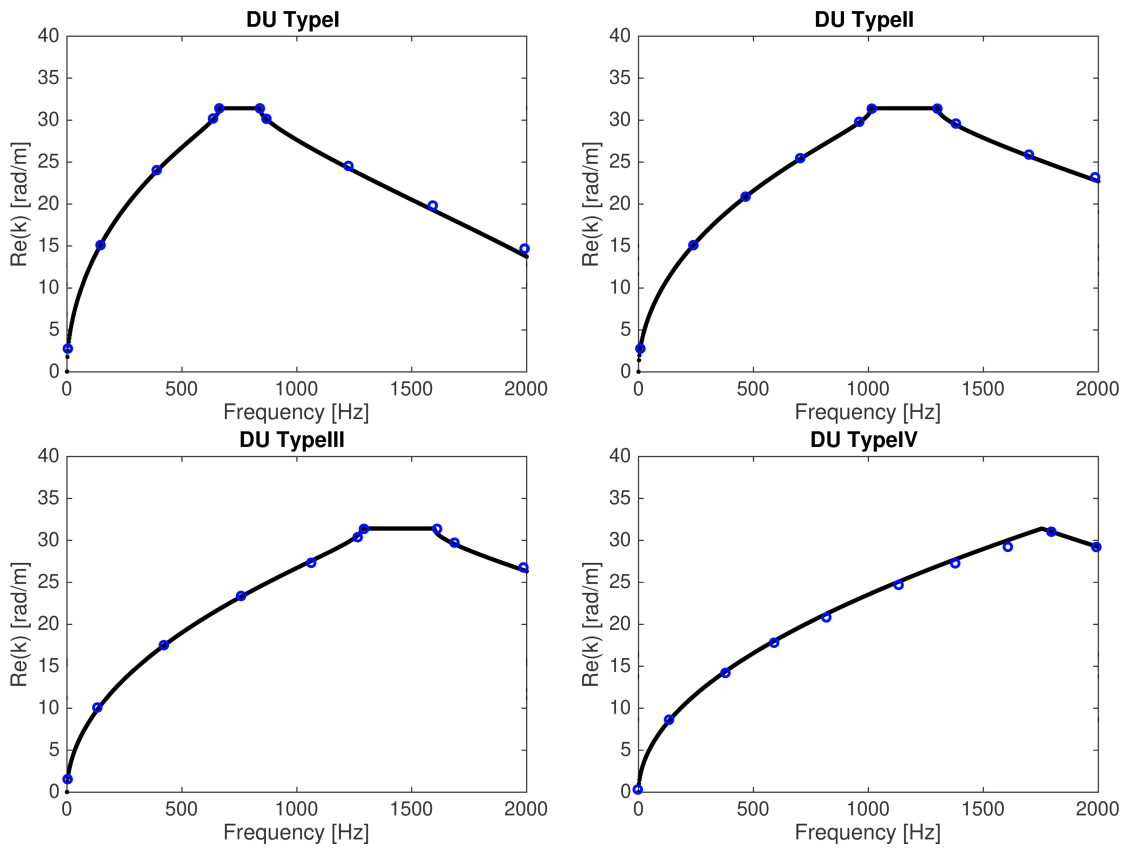


Figure 3.9: Duple Unit cell results with comparison with [9] (blue circles)

and, for all of them, a shift to higher frequencies is clear, moreover the stopbands width increases with the decrease of the ratio between the two dimensions. Type IV does not present any stopbands like the Double Unit in Figure 3.9.

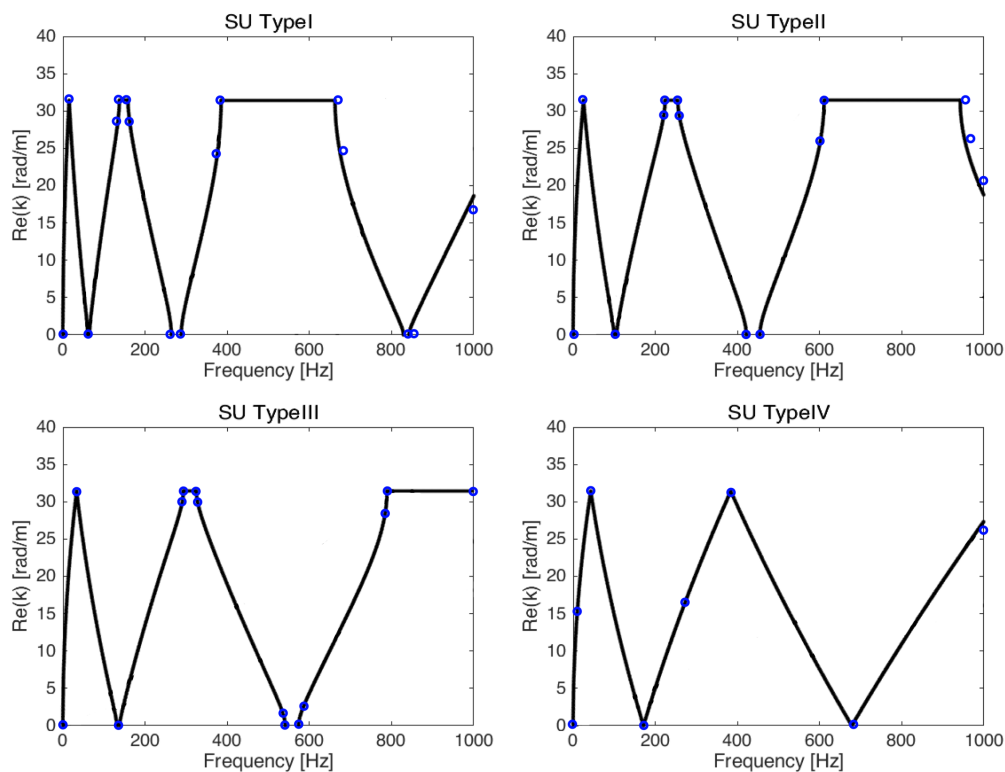


Figure 3.10: Super Unit cell results with comparison with [9] (blue circles)

Material variations analysis

After the analysis of the performance related to the variation of the geometry previously addressed, the material-related properties of structures will be approached by using the same Fibonacci structure used in the previous section, and the related research [9]. In this case, all the subunits have the same dimensions as case IV in Figure 3.2 with the A subcells always made of steel, while the B subcells material varies for each of the three cases covered. All the materials are displayed in Table 3.2.

Case	Cell	Material	E [GPa]	ν [-]	ρ [kg · m ⁻³]
-	A	Steel-A36	200	0.26	7800
1	B	Al 2045-T4	73	0.33	2700
2	B	Magnesium	45	0.35	1700
3	B	Copper	110	0.355	8960

Table 3.3: Material variation of the two subcells

The Fibonacci sequence is used to decide the order of A and B cells in the unit to propagate. The sixth order Fibonacci sequence is used to order the thirteen subcells into a complete cell. The resulting cell is 1.3 meters long with the subcell arranged in **ABAABABAABAAB** order. Same as the structure in the previous section, each subcell is modelled as a B4 element along the length and the section is modelled via a Taylor expansion of the second order. Then the input files are elaborate by the CUF package and the resulting matrix are then used by the WFEM script to extrapolate the spectrum and identify the stopbands.

In the following three figures, the results of the analysis are presented: the most prominent part of the figures are the blue zones, that highlight the stopbands in the structure. Figure 3.11 will be used as baseline for the comparison. Here six stopbands are present: the most prominent is the third that extends from 6.5 to 6.8 kHz, while three other visible stopbands appear near the 5 kHz, 8.5 kHz and 10 kHz.

In Figure 3.12 one more stopband is presented around 4 kHz and generally all the stopbands in the first case are wider, with the widest going from 6 kHz to 7 kHz. Comparing this case to the first, it is clear that the proportional decrease in Young's module and Poisson's module causes the stopband to widen without translate to other frequencies.

In the third case, represented in Figure 3.13, most of the stopbands disappear with the only one remaining that is very narrow. This case presents a uneven increase in the material properties, especially the Young's module. In particular, the result of this increase is the translation to higher frequencies of the deadbands.

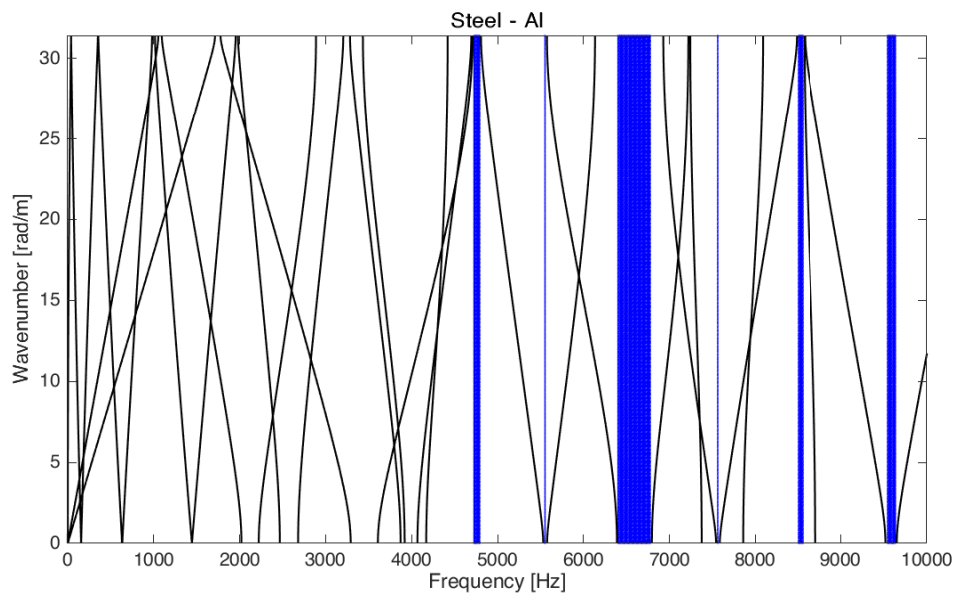


Figure 3.11: Case 1 - Spectrum with highlighted stopband

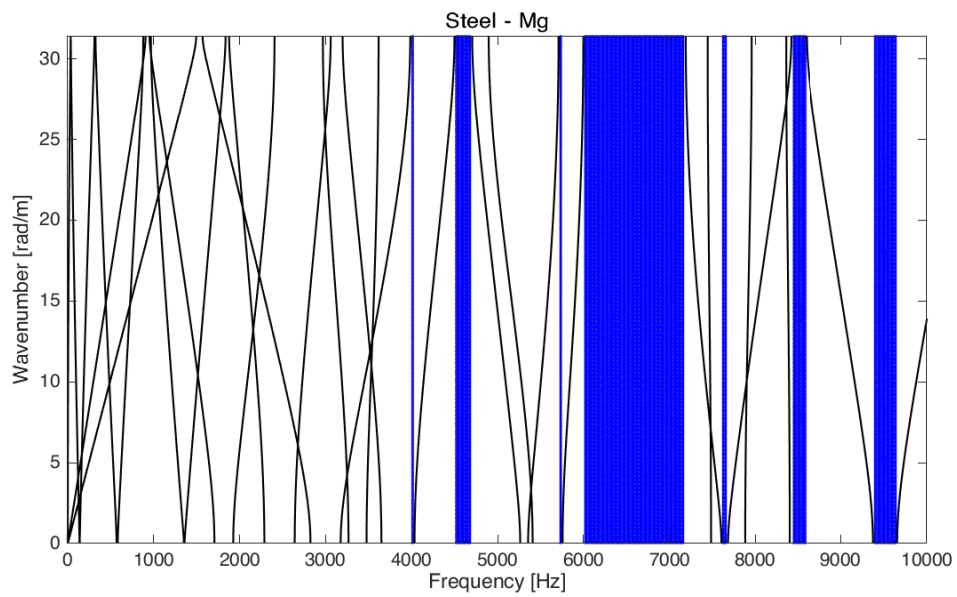


Figure 3.12: Case 2 - Spectrum with highlighted stopband

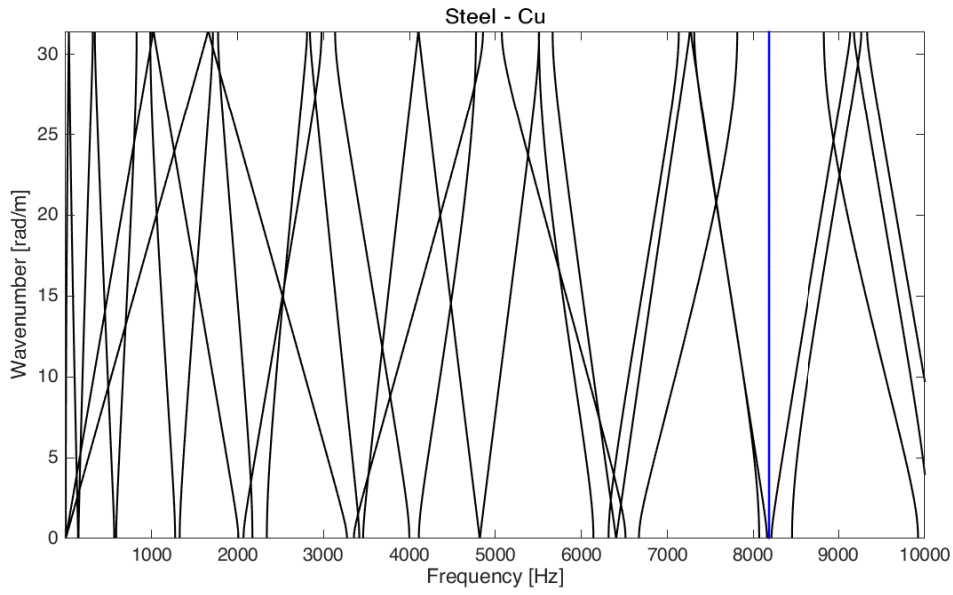


Figure 3.13: Case 3 - Spectrum with highlighted stopband

Mixed section beams

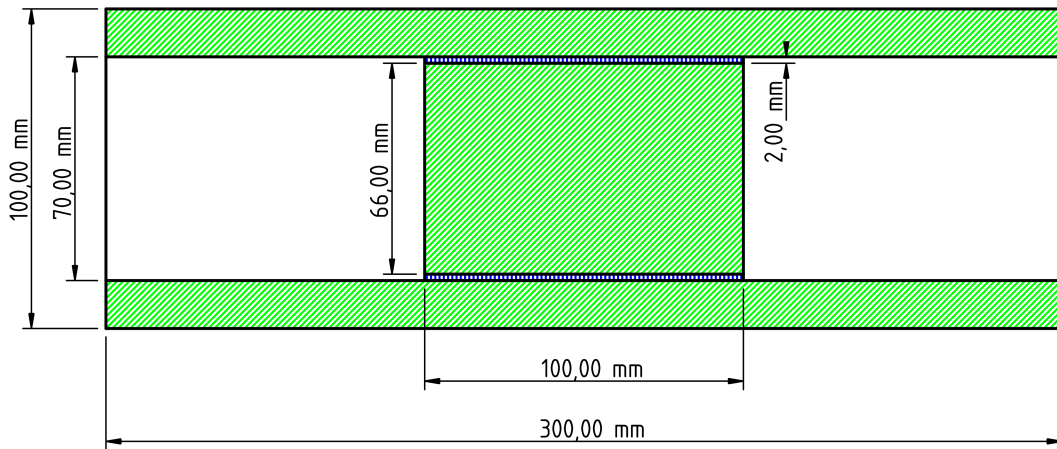


Figure 3.14: Section view of the Configuration B beam

In this section two beams will be analysed. The first is composed of two cubic subunits, one hollow and one solid, both made of steel. For the second beam, the hollow subunit is maintained, while the solid one is exchanged with a dampened

subunit. In particular, this variation is made using the hollow subunit as the outer sleeve with a thin layer of low Young's module and density material (epoxy) to connect it to the central core, also made of steel. The hollow/solid configuration will be identified as 'Configuration A', while the other as 'Configuration B'. In Figure 3.14 the section view of this dampened beam is presented with all three components visible: the outer sleeve and core are highlighted with green and the adhesive layer between them with blue. For both the beams, the hollow subunit is two times longer than the solid/glued ones to balance the weight of the two subunits.

As for the previous models, the input files are prepared with the three sections (hollow, solid and glued) modelled with a second-order Taylor expansion and the beams made of three B4 beams in the configuration hollow-filled/glued-hollow. Then the inputs are elaborated by the CUF package and the matrices are passed to a MATLAB script to propagate the structure to obtain the results in Figure 3.15 and Figure 3.16.

On Figures 3.15 and 3.16 the two variations of vibrational performances differ: the addition of a viscous layer in the structure lead to a more complex behaviour with less clearly defined stopbands and more modes across the lower frequencies.

One interesting aspect that can be explored with this simple structure is the dependency of the results on the discretization choice. In particular, the same structure is discretised with a higher order (third) Taylor expansion and a Lagrange expansion (LE9) for the section, while maintaining the B4 discretisation for the length. Most of the difference between the various discretisations is in the number of DoF needed to describe the structure: 180 for the TE2, 300 for the TE3 and 1356 for the LE. With the increase in complexity, a rise in simulations resource comes as well. In this case, the last batch, i.e. the Lagrangian expansion requires a decrease in the number of probing points to execute in a reasonable time, from the 200 used for both the TE to just 15 divisions for the LE model. This decrease in points used bears results difficult to compare to the ones from the more refined analysis but still readable enough to compare.

From the polished results in Figure 3.17, 3.18 and 3.19, a big difference can be seen between the various discretisations. The results suggest the deep relation between the performance of the WFEM algorithm and the discretisation used for

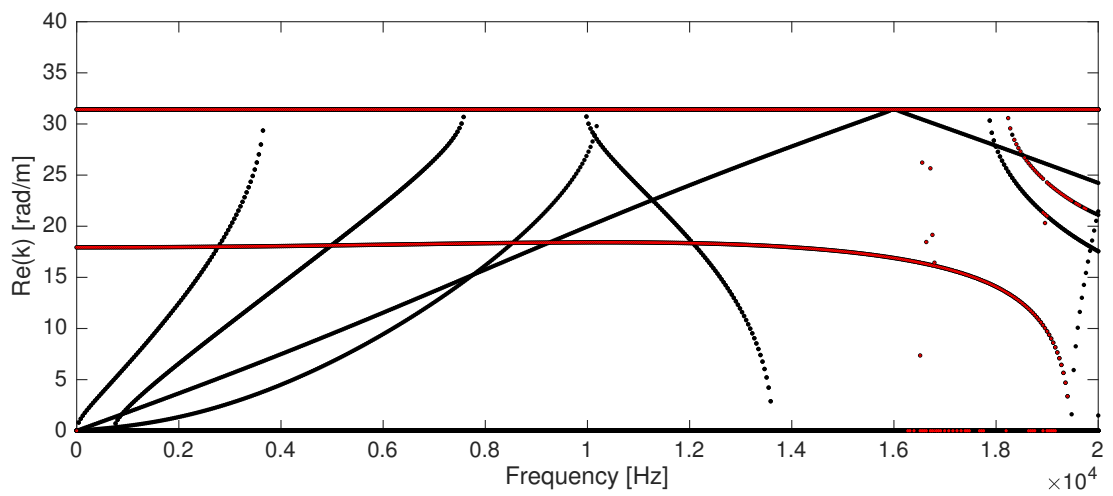
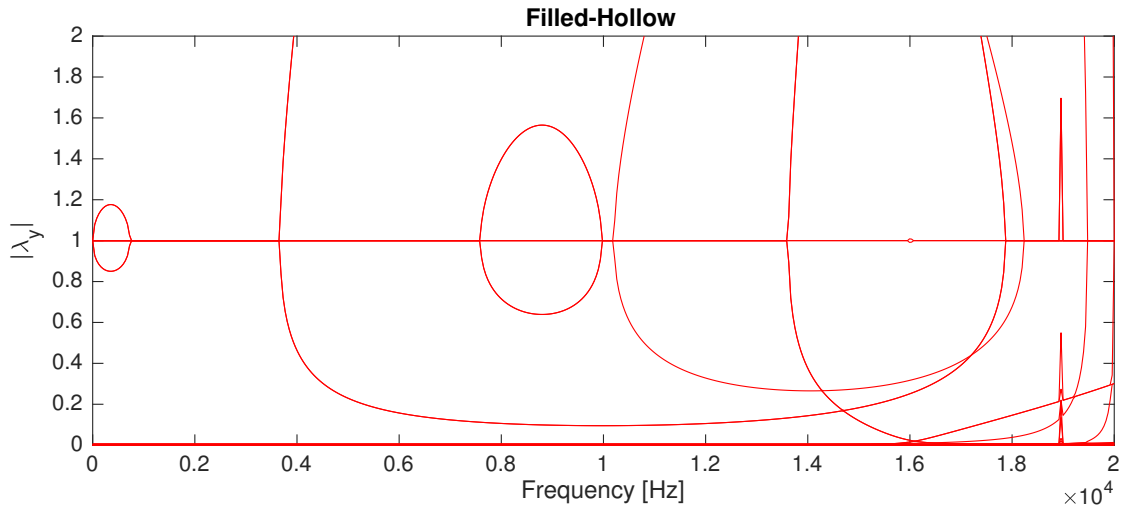


Figure 3.15: Configuration A

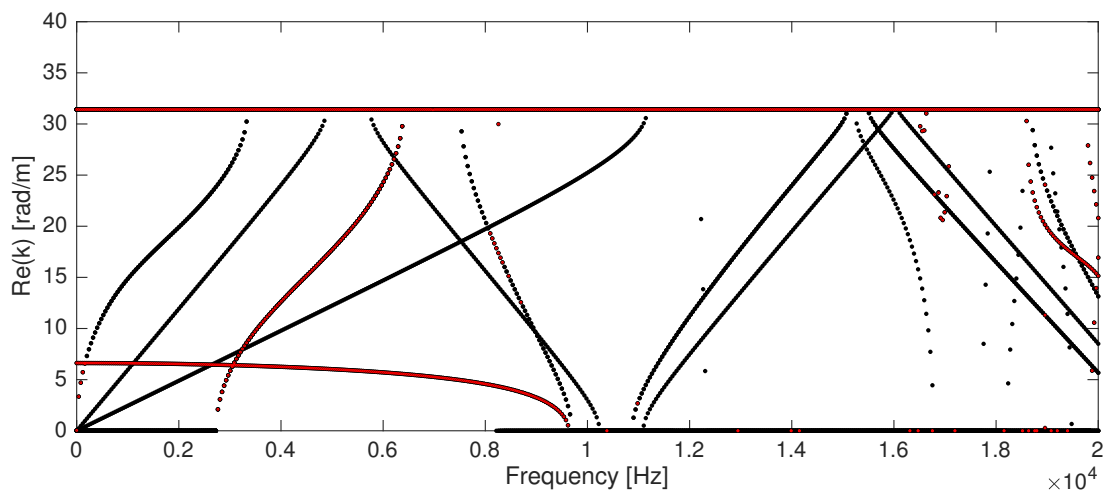
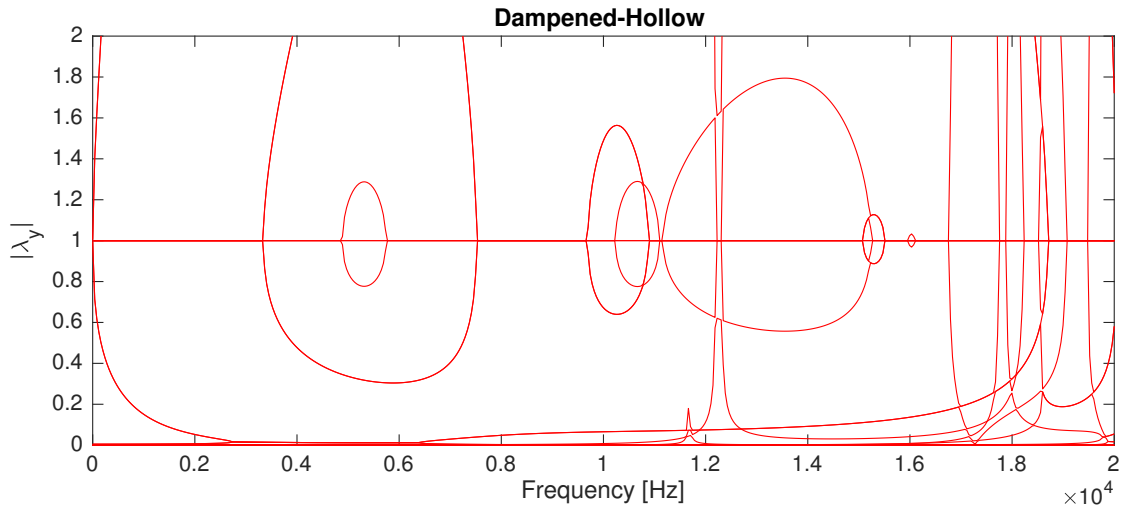


Figure 3.16: Configuration B

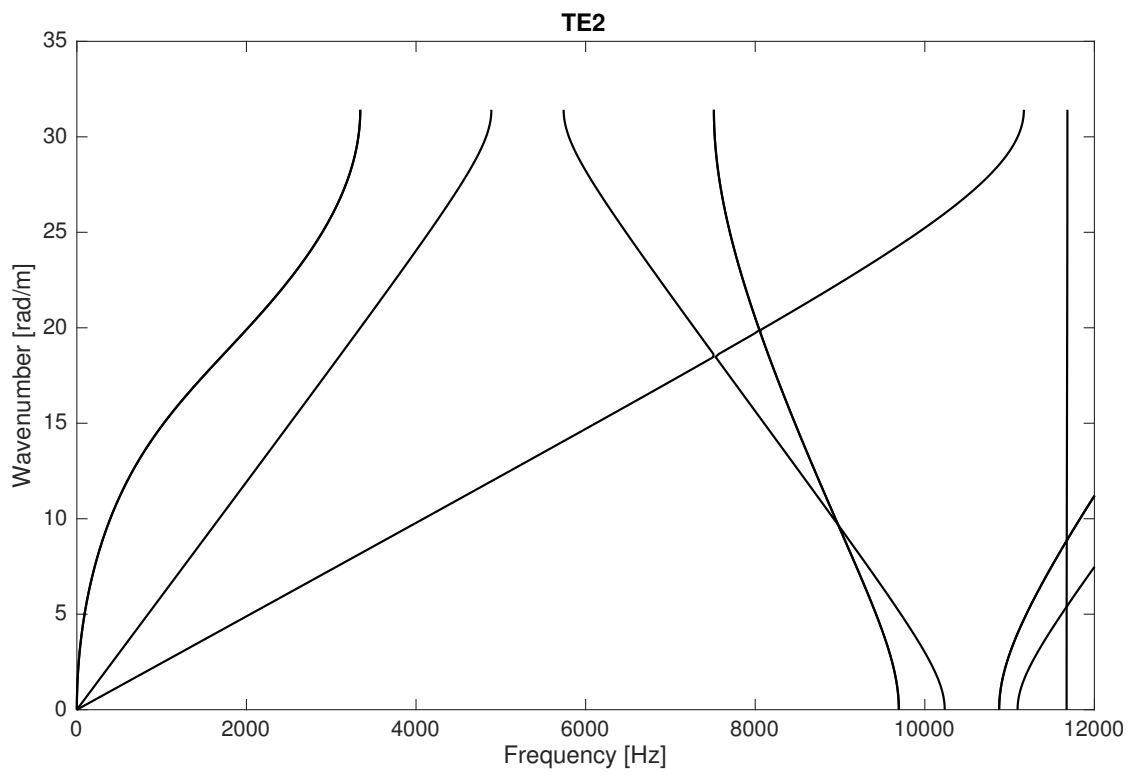


Figure 3.17: Spectrum for the TE2 discretization

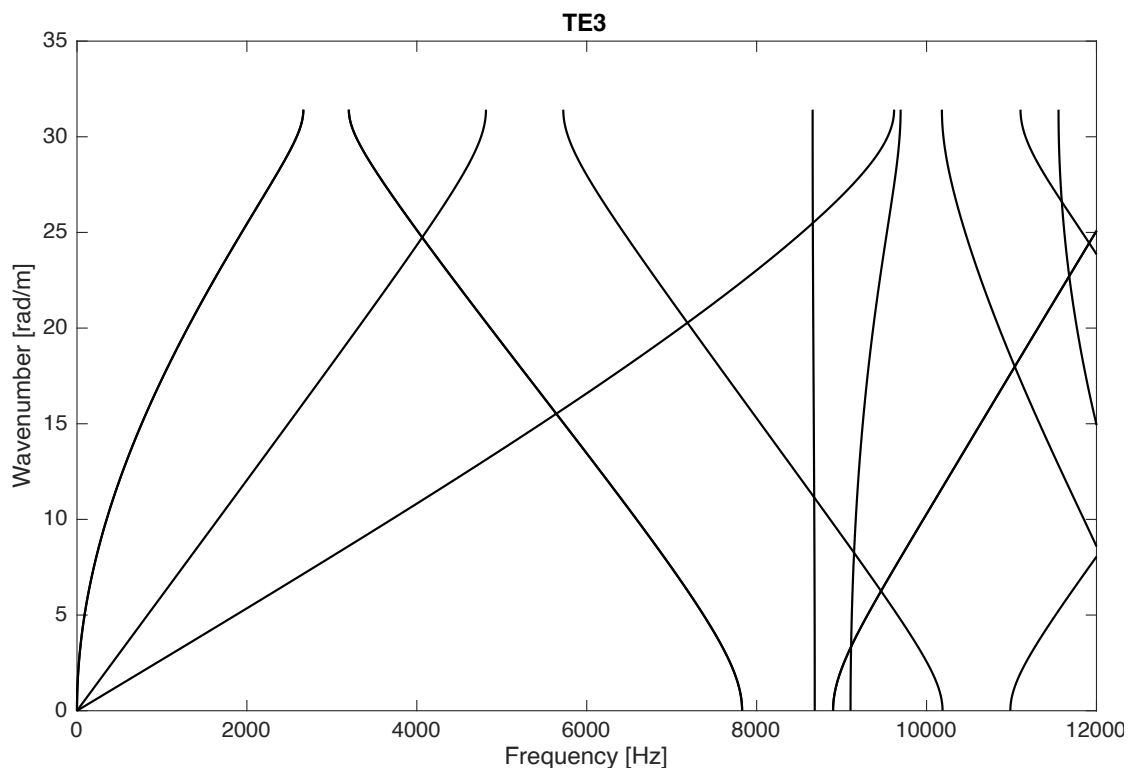


Figure 3.18: Spectrum for the TE3 discretization

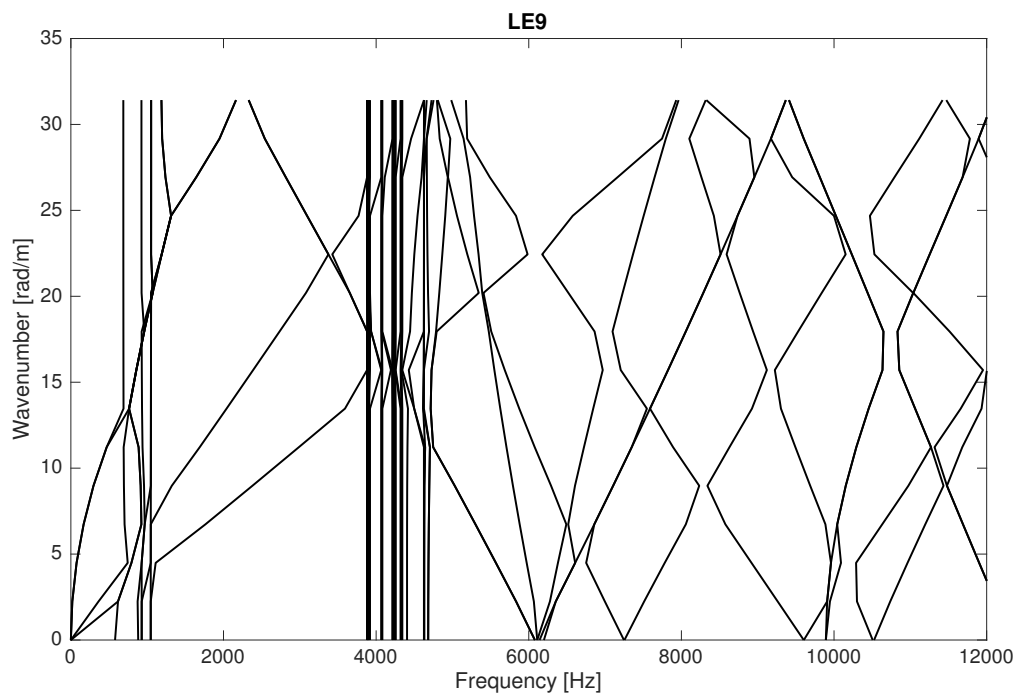


Figure 3.19: Spectrum for the LE9 discretization

the structure.

Chapter 4

Wave propagation analysis

4.1 Proposed configurations

After a modest amount of analysis to understand the WFEM algorithm strengths and weaknesses done in the previous sections, this chapter will focus on the structure already treated in the previous part of this document. The gate structure will be analysed with the WFEM algorithm in order to answer the vibrational problem and finally propose some case to be used to take advantage of the structure properties.

Most clear course of action is to feed the structural matrices of the same model analysis on Chapter 2. The results from the analysis done on the previous chapter a more efficient structure can be assembled in order to optimize future analysis, three options were proposed to optimize the model and easing future analysis:

1. Forcibly reducing the number of DoF changing the discretisation used for the model. This option can lead to erroneous results due to the deep dependence of the WFEM algorithm on the discretisation proved on the previous section. However, this option can be proven possible to obtain the correct result with some proper analysis.
2. Using an outdated bidimensional model of the structure allow to greatly reduce the DoF of the model at the cost of the loss of one of the dimension of the original structure.

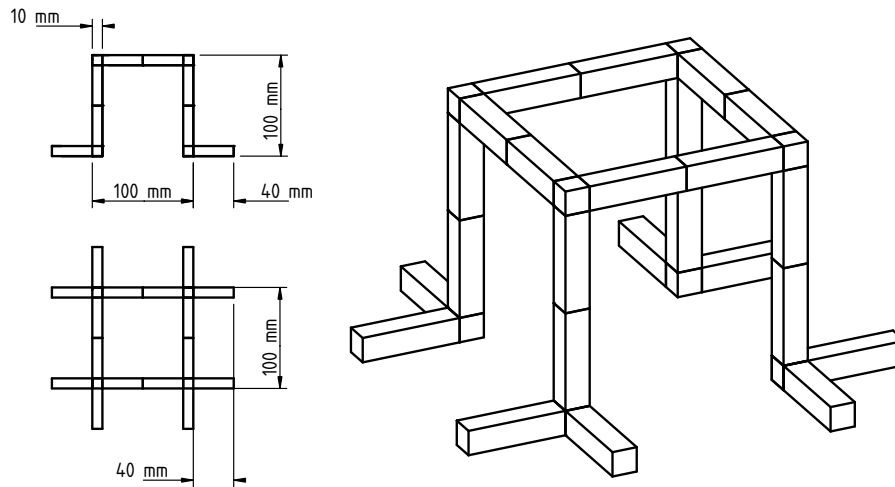


Figure 4.1: Drawing of the 1X1 configuration with dimensions

3. By exploiting the powerful propagation of the WFEM to reduce the structure to the most basic element, the number of DoF feeded to the algorithm can be greatly reduced, allowing the code to run on a typical machine. Unfortunately the structure analysed in the previous chapter can not be further reduced, so a new similar structure was proposed to check the viability of this option.

Besides the proposed options capability to greatly reduce the DoF to a more manageable number, the algorithm is still unable to produce results in a manageable amount of time, so it is necessary to reduce the definition of the analysis to tens of probe points in order to obtain the results. This additional action causes the result to be less smooth, while some details, like the intersection between different modes, can become less clear.

As in the previous analysis, all the options start with the modelling of the structure at a nodes level, then the obtained files are used by the Mul2 program to output the structural matrices to be feed to the WFE MATLAB script. The

last phase is to elaborate the output result from this last one script to create the needed representations.

4.1.1 Option 1 - TE discretisation

Using the Taylor Expansion discretisation for the tridimensional gate structure allow to greatly reduce the DoF of the model, up to a degree were is possible to analyse the structure with a high definition without a high computational time. The results from this work are well defined and easy to read, but in order to verify the correctness of the result obtained from this option, it is important to compare them with the ones derived from the second option, as they are produced with a more precise Lagrange Expansion discretisation.

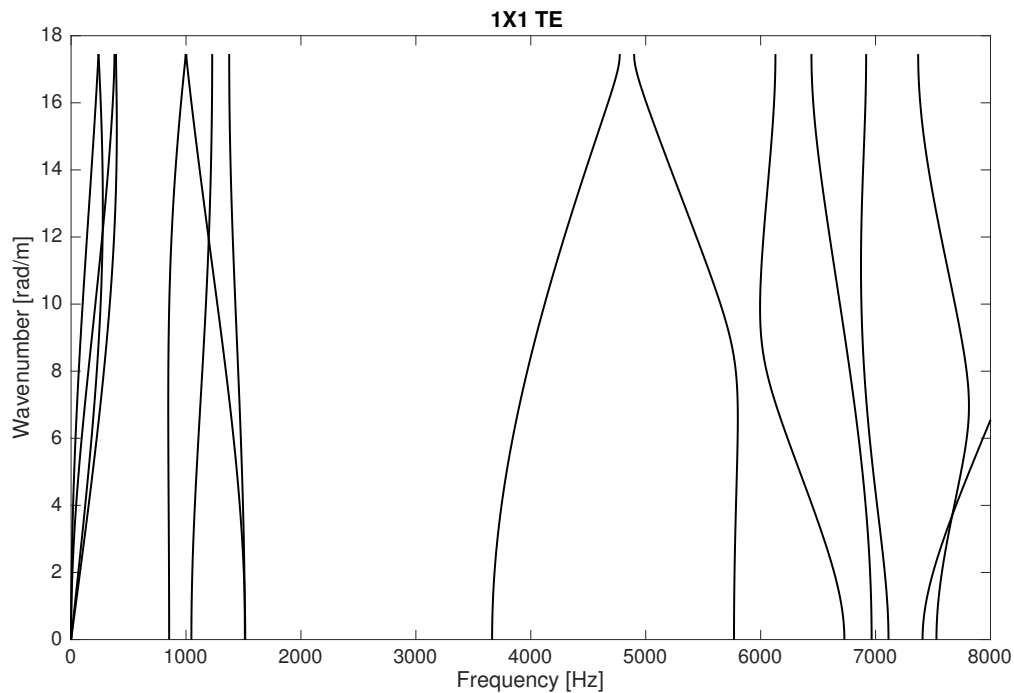


Figure 4.2: Result of the 1X1 configuration with Taylor Expansion analysis

4.1.2 Option 2 - 2D gate structure

In this option the width of the structure is reduced to a single spar. The structure is still a tridimensional one but the complexity is greatly reduced due to the shrinking

of one dimension. This expedient allow to use the Lagrange Expansion for the analysis without concerning about the time necessary to complete it. However, even with the reduction due to the loss of one dimension, the already mentioned decrease of definition is needed to output a result with a manageable execution time. For this reason the results are not as smooth as the ones presented during the Option 1 and some guessing is needed to identify the intersections between modes.

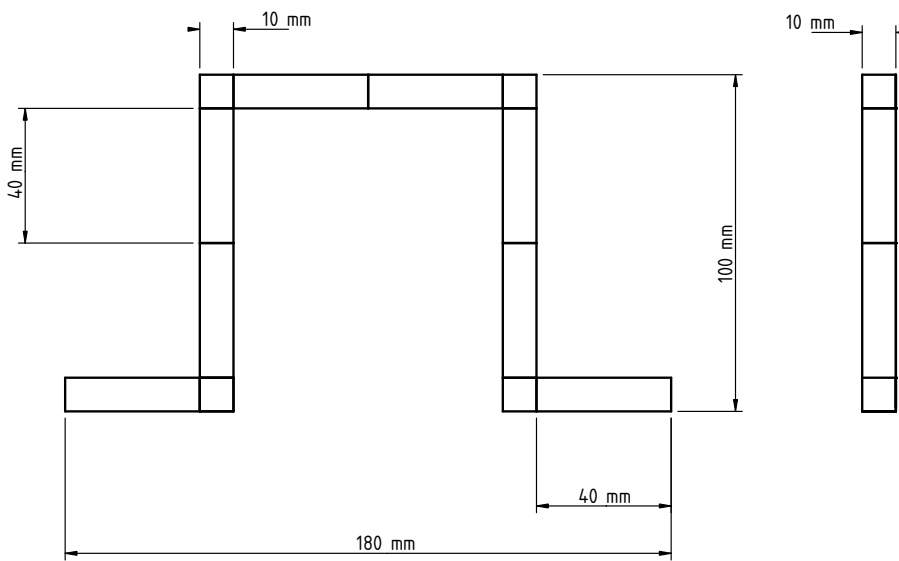


Figure 4.3: Drawing of the 2D configuration with dimensions

Each cell on the structure represented on Figure 4.3 is discretised with a L16 element. The same cells are used to discretise the model for the third option, shown on Figure 4.5. The second option model is made with a total of 12 elements, of which four are cubic. The third ones is made of the same 12 elements but in this case only two of them are cubic.

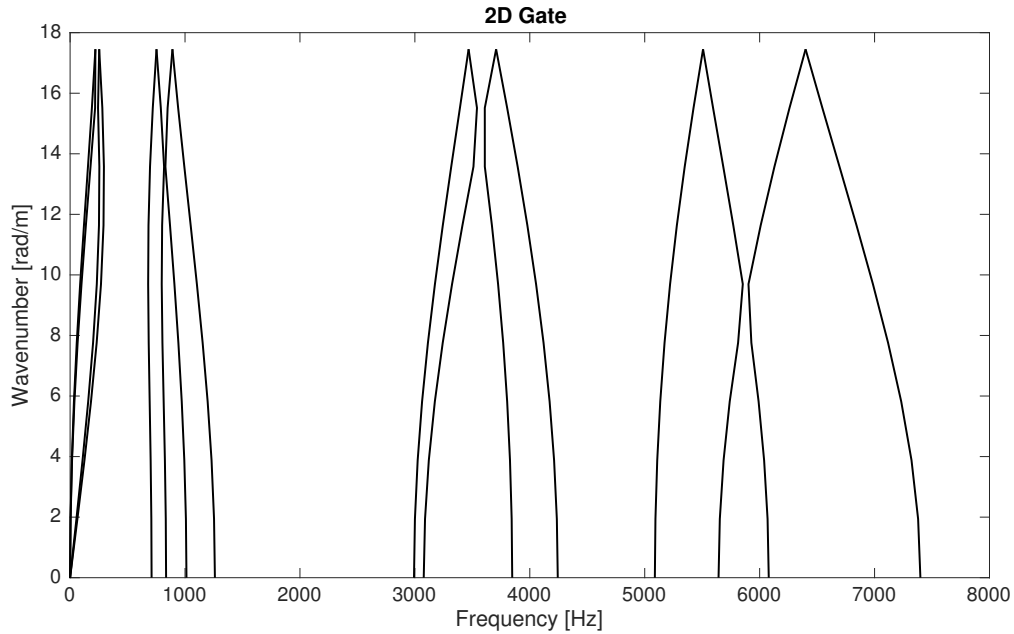


Figure 4.4: Result of the 2D gate analysis

4.1.3 Option 3 - 3D cube structure

WFE method pivots on the propagation of a structure to solve the vibrational problem, so big structures can be easily analysed by reducing the structure to its basic element. Unfortunately the original concept is too complex to be further decreased, so a similar but simpler structure is created to test the reduction. This test structure is made by a series of interconnected cubes that can be easily reduced to a single edge with eight protruding half edges from the two extremities of the rod. This option allows to greatly reduce the DoF of the structure without missing its tridimensionality. The price to pay for this simplification is the difference between the original and the new structure, but it may be possible to adapt the WFEM math to allow mirrored propagation, in order to fully analyse the correct structure using a more reduced model.

4.2 Cube core sandwich panel

The third option also allows to assemble a sandwich panel by adding two plates over and under the cube structure acting as a core. This configuration is represented

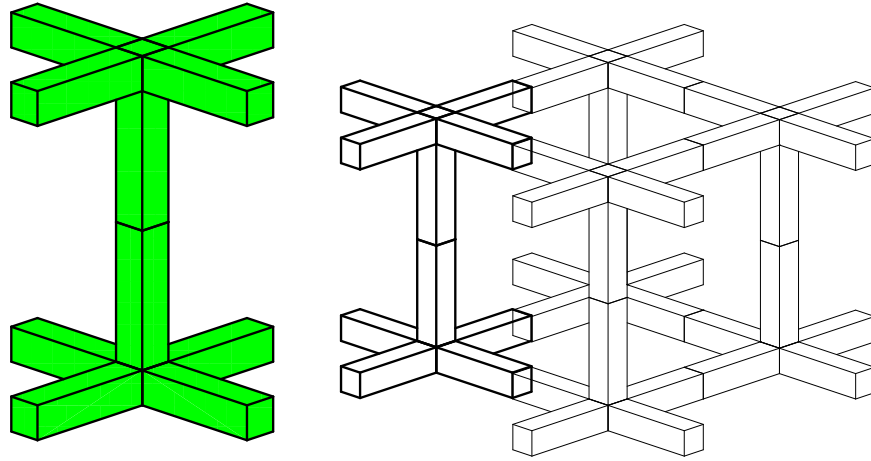


Figure 4.5: Drawing of the Cube configuration with propagation

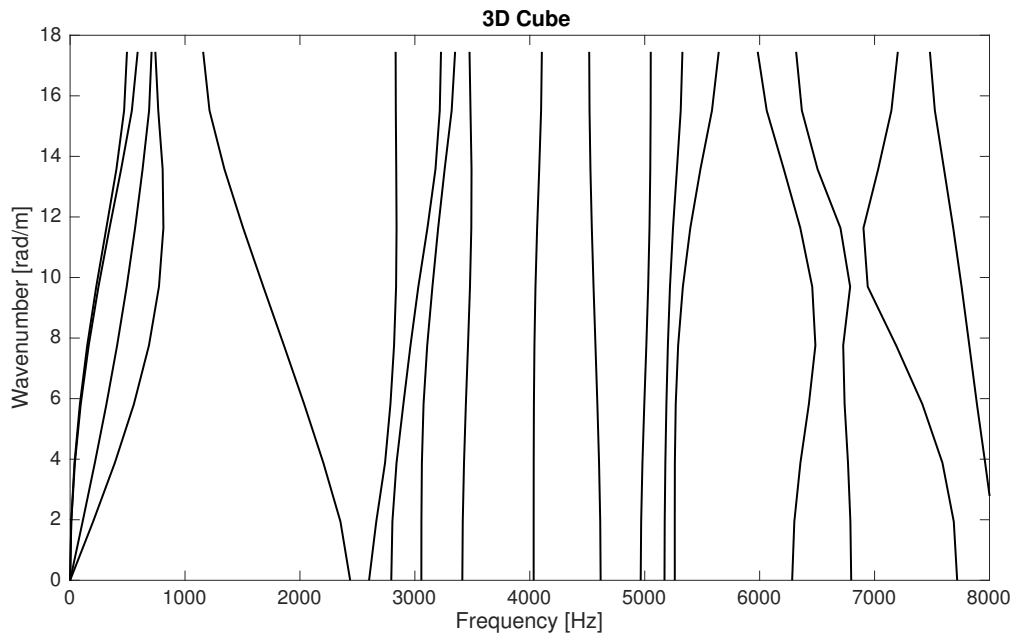


Figure 4.6: Result of the 3D cube analysis

on Figure 4.7. This structure is made up by a central core taken from the previous third option and two aluminium plates. During the analysis on this section the material which the core is made will be varied to acknowledge the performance of each combinations.

Three materials will be used to analyse the performance of the structure, all the materials are commonly used in the aerospace industry: while aluminium and steel are the backbone of every flying structure from the introduction of metal frames, the third chosen material, aramidic fibers, its a relatively recent introduction to the field. Most used as core for traditional sandwich plates in a honeycomb configuration, they are also used as fiber were additional shear strength is needed. Recent development of additive manufacturing have made available this fibers properties for more complex tridimensional structure, impossible to manufacture with the traditional lamination methods. The materials properties are summarized on Table 4.1.

Material	E [GPa]	ν [-]	ρ [kg · m ⁻³]
Steel	210	0.30	7700
Aluminium	75	0.33	2700
Aramididic Fiber	1.7	0.30	1100

Table 4.1: Sandwich core materials

The discretization for this batch of analysis is similar to the ones used for the third option. The two additional plates in the structure are discretized along the cross section with three LE16 cells while three B4 are used to discretize the depth of the plates. In the next sections will also analyse the same structure with Taylor Expansion instead of Lagrange Expansion and the result of the two will be compared one to another. The usual workflow are used for the simulations where firstly the model is created and successively fed to the CUF package for computation of the mass and stiffness matrices. Afterward these two matrices are used by the WFEM code to extract the results which are finally produced as graphs.

On Figure 4.8 is represented the result from the steel core sandwich. This

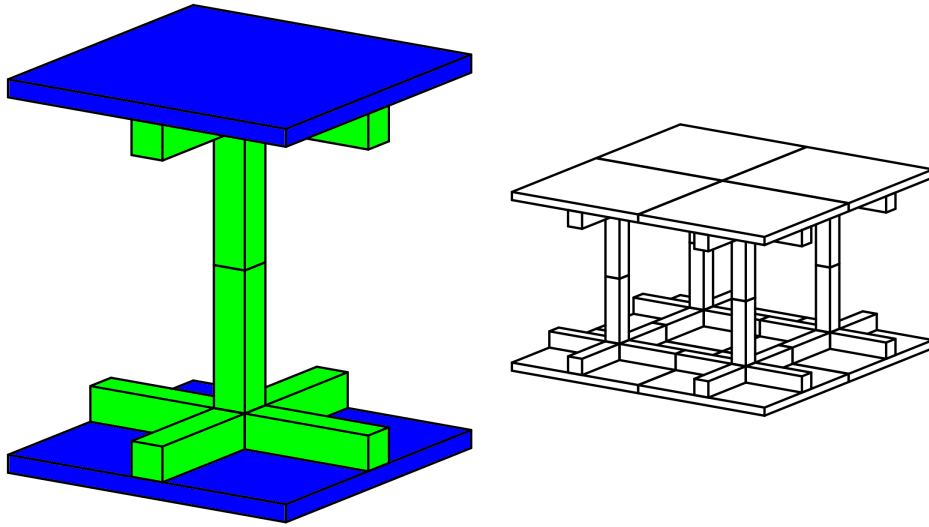


Figure 4.7: Sandwich configuration

configuration is obtained simply by adding the two aluminium plates to the steel core from Option 3. On this Figure the range below 8000 Hz is depicted to allow an easy comparison with the result obtained from the core alone on Figure 4.6. The sandwich configuration features the same four modes starting from the origin, however the sandwich configuration are wider and one of them have an unexpected behaviour where the mode rise to a wavenumber of four rad/s and then slowly raise to max when reaching 20000 Hz. Similar behaviour can be seen for the following modes where the distribution and evolution is similar within the two configurations while the intersections with the horizontal axis is shifted to higher frequencies.

Figure 4.9, Figure 4.10 and figure 4.11 contain the results from the analysis with different core materials. These graphs allow to compare performance of the structure between difference combinations of materials. All the analysis have a common features: three (aluminium) or more modes (steel and fiber) starting with a frequency of zero Hz; also, there is a strip around 25000 Hz where the modes are more spaced than other frequencies. This last common feature from all

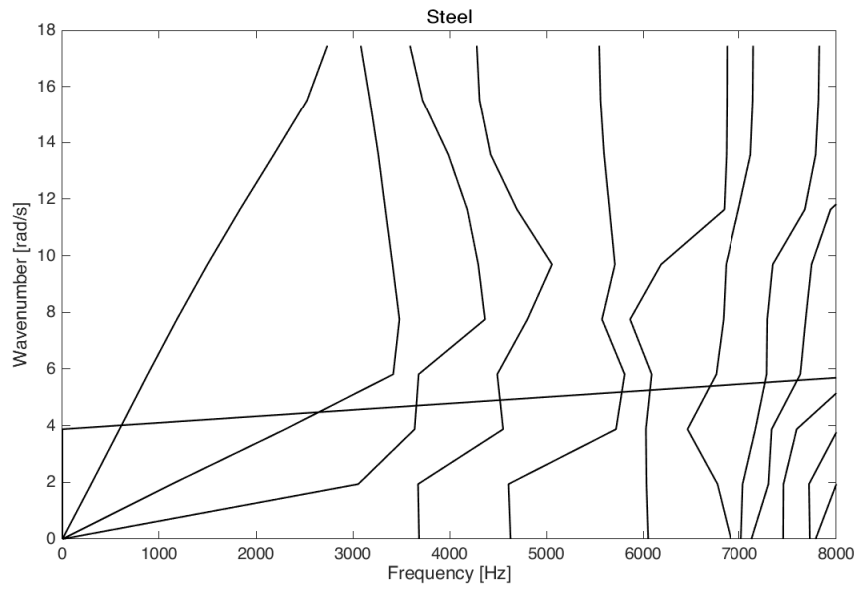


Figure 4.8: Result of the sandwich analysis for comparison with simple cube configuration (steel core)

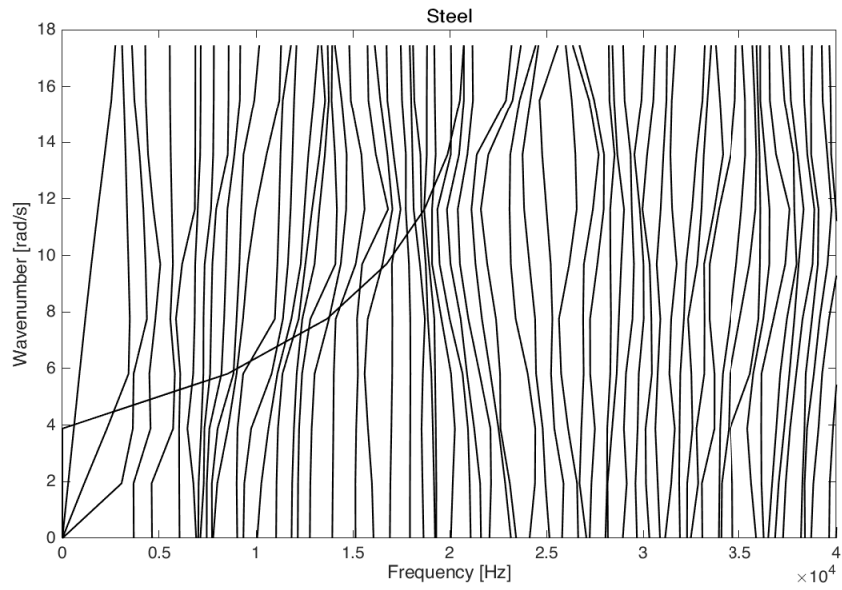


Figure 4.9: Result of the sandwich analysis with steel core

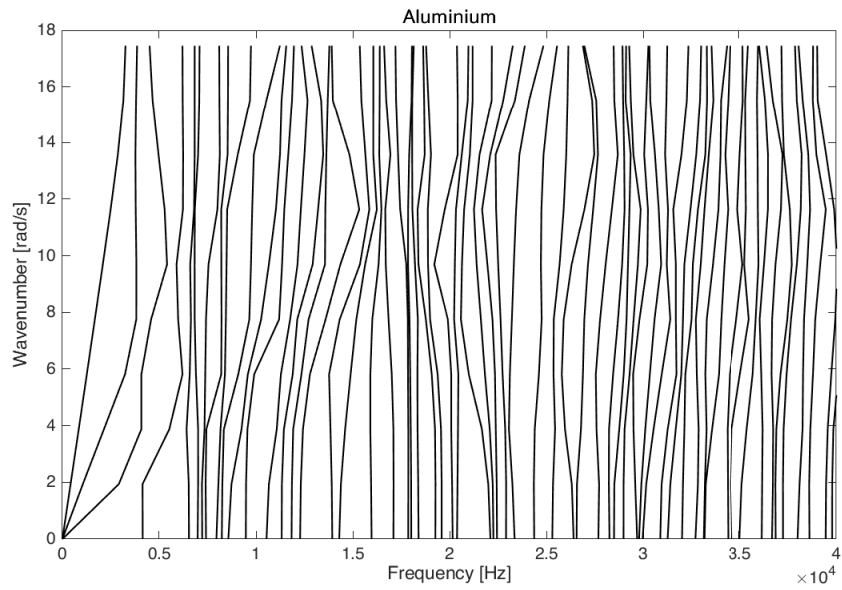


Figure 4.10: Result of the sandwich analysis with aluminium core

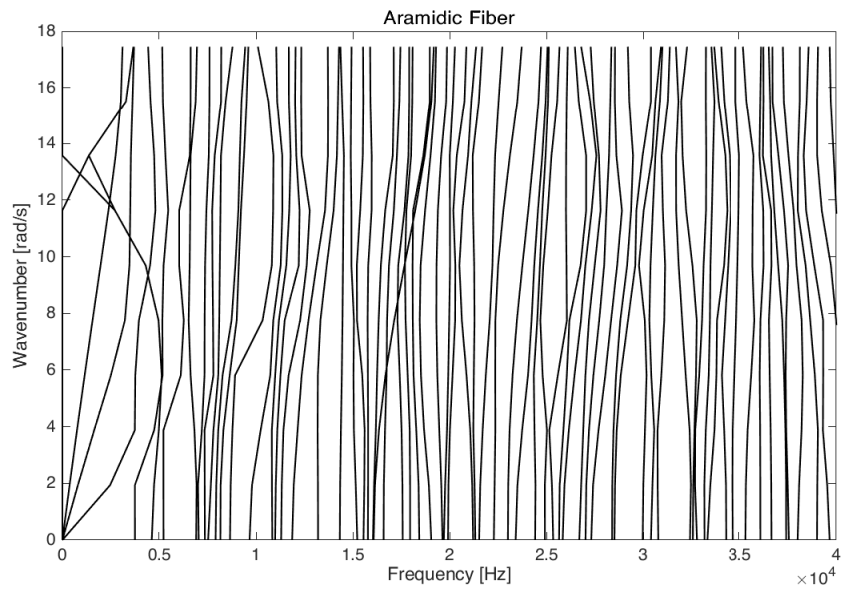


Figure 4.11: Result of the sandwich analysis with aramidic fiber core

the core materials can be related to the geometry of the structure rather than to the material composition itself.

On the other hand, the steel and aramidic cores have a complex feature in the low frequencies where a mode stand out compared to the others. For the steel is the already described parabolic feature which cuts along the graph from the origin to around 20000 Hz. Meanwhile, the aramid fiber result shows a mode starting around 5000 Hz come back to the y axis. Those features will be better analysis within the next section where another discretization will be used to gather more results.

4.2.1 Results with Taylor Expansion

The analysis within this section uses the same structure and materials, but a different discretisation is used. Indeed, the next graphs are based on a Taylor expansion instead of a Lagrange expansion. In addition, various order of Taylor Expansions are tested to provide a better coverage of the behaviour of the structure with different materials. The workflow for generating this graphs is equal to the one used for the Lagrange expansion, but with a slightly different input files and an additional step. On this additional step the results from the WFEM are further processed by the CUF package to generate a visualisation of the modes available thru the ParaView software.

Firstly the features shown by the LE graphs with steel and aramidic fibers are explored with the aid of this new discretisation.

On Figure 4.12 and Figure 4.13 results from the first-order and fifth-order Taylor expansions are represented. The first-order graph contains less modes due to the reduced number of DoF for the low order of expansion. However, the four modes starting from the origin are visible in this graph. The fifth-order graph is more densely packed with modes and also the parabolic feature is clearly visible among the lines. Rather than starting from a wavenumber of four and then steadily increase, reaching the maximum value at 20000 Hz like on the LE analysis, in the TE case the slope is steadily increasing from the origin to around 10000 Hz with a more wide parabolic development. In addition to this features, another steady path is visible: a constant rise from origin to around 25000 Hz runs through the graph.

On Figure 4.14 and Figure 4.15 results from the first-order and fourth-order

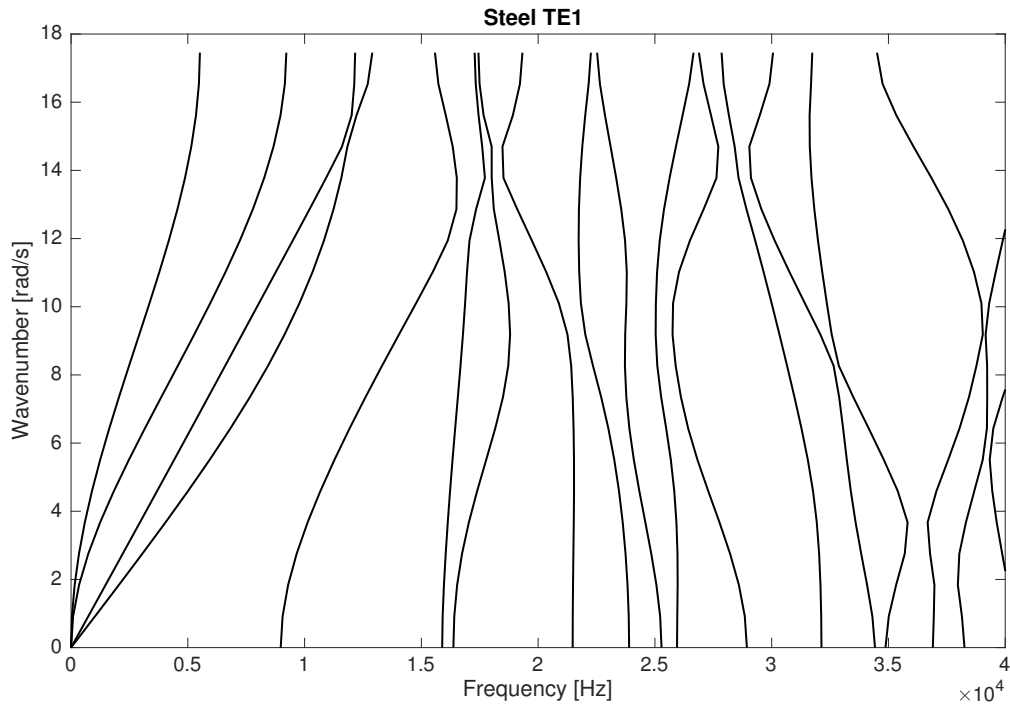


Figure 4.12: Result of the sandwich analysis with steel core and first-order Taylor Expansion

Taylor expansions are represented. With this core material, the choice to stop at the fourth-order expansions is the result of an increasing instability of the data with the order increase. This instability is visible on Figure 4.15 around 6000 Hz and 34000 Hz, where the two modes repetitively exchange paths. To circumvent this instability the modes analysis is done on a third-order Taylor expansion: with this order the instabilities are outside of the graph range.

Same as the steel core Taylor analysed above, the aramidics core presents the same number of modes starting from the origin of the graph. This feature is present on both the first-order and third-order results. The second unique feature of the LE results is also shown on the TE data, although it is visible only on the fourth-order graph. On the Lagrange results on Figure 4.11 there is a mode that starts around 5000 Hz and then turns back to the wavenumber axis near 14 rad/s. Instead, on Figure 4.15 a similar turn around feature can be seen starting around 6000 Hz and then going back to less than 3000 Hz.

The common feature between all the core materials on the LE analysis was

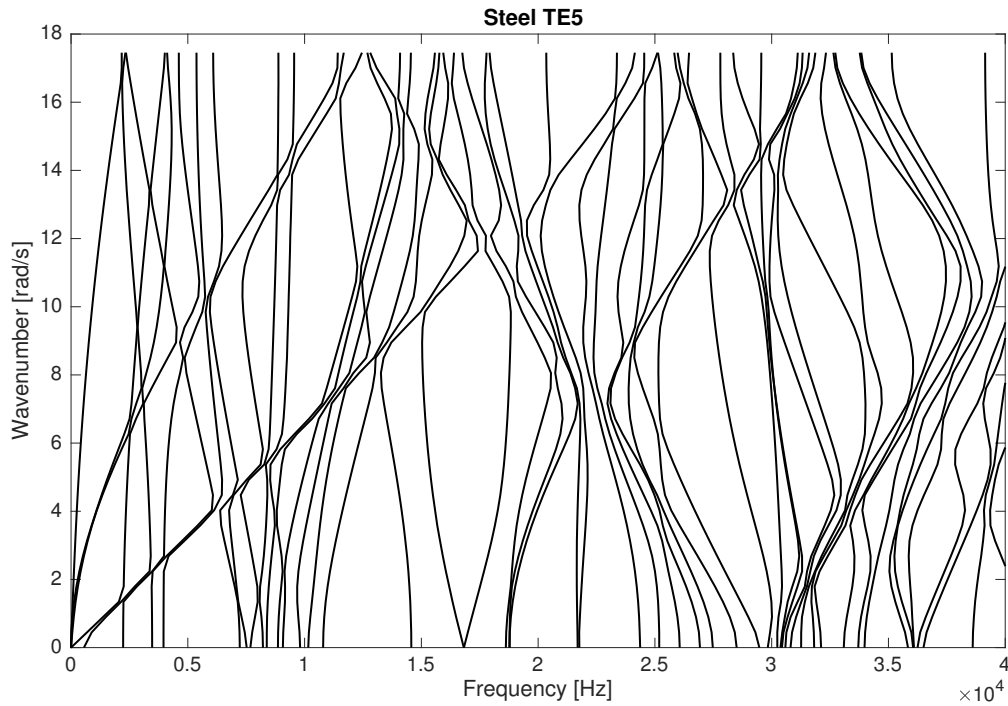


Figure 4.13: Result of the sandwich analysis with steel core and fifth-order Taylor Expansion

a scarcity of modes on the frequencies range around 25000 Hz. This same lower density can be seen on the TE results, still in this second case the range is slightly off: at higher frequencies for the steel core, while at lower ones for the aramidic core structure.

Modes analysis

On this section modes analysis is used to investigate the three core materials properties. For this study the first ten modes of each configuration is extracted and represented with a tridimensional model superimposed to a black lined wireframe of the original structure. Each mode is identified by a letter from *A* to *J* and also a reference graph for each material is featured to identify the position of each one. Moreover, for each material the represented modes are extracted from mid of the wavenumber scale, a little over eight rad/s. This uniformity allows comparison even between different materials cores.

The first option analysed is the steel core one. On Figure 4.16 the reference

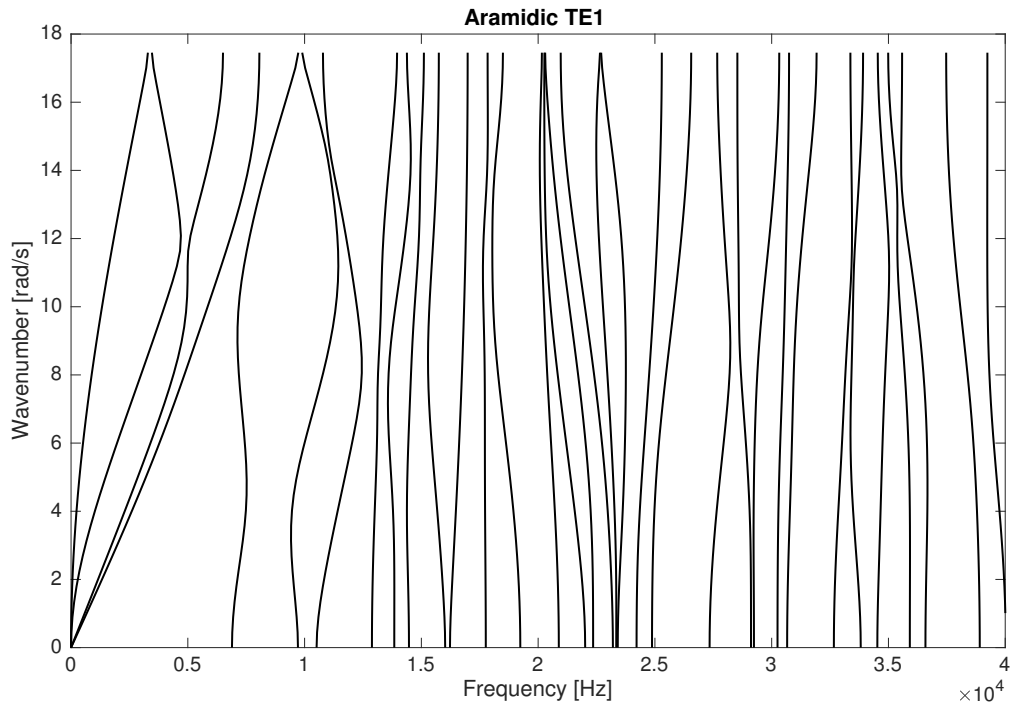


Figure 4.14: Result of the sandwich analysis with aramidic fiber core and first-order Taylor Expansion

graph is shown, with a limited frequencies range than the one used on the previous graphs. This choice is made to encapsulate all the first ten modes and the same frequency range will be used for the next reference graphs.

On Figure 4.17 the first ten modes of the steel core structure are represented, for each mode a deformed model and a black wireframe of the original geometry are provided. The deformation gain is selected for each image to highlight the movement of the structure without missing the support from the wireframe to better understand the deformation. The axes used for the description of each mode are: X axis from right to left of the page; Y axis pointing into the page; Z axis pointing up. The models are described on Table 4.2

Most of the modes identified for the steel core structure are bending ones. For this particular combination two main trends can be seen: from the bottom the first to appear is a rectilinear line starting from the origin and the second, just above the first, is a parabolic curve originated from the same point as the previous one. The extraction point for the modes happens to intersect the second one, the

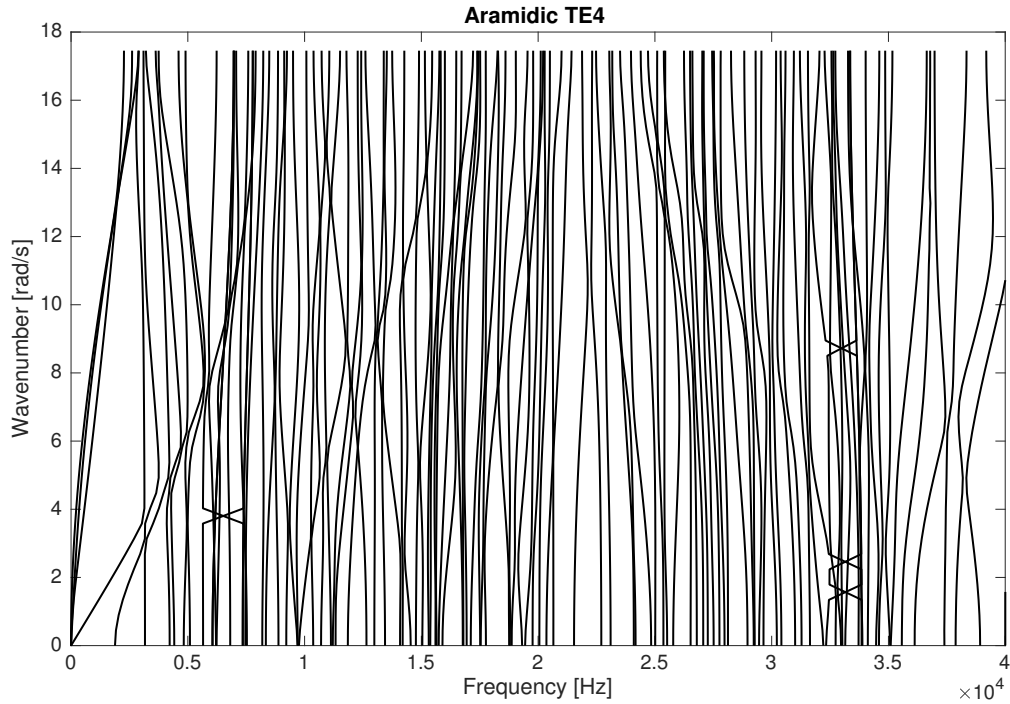


Figure 4.15: Result of the sandwich analysis with aramidic fiber core and fourth-order Taylor Expansion

Mode	ref	Description
<i>A</i>	4.17a	Global bending mode along <i>Z</i> axis
<i>B</i>	4.17b	Local bending mode along <i>Y</i> axis
<i>C</i>	4.17c	Global bending mode along <i>X</i> axis
<i>D</i>	4.17d	Global torsional mode along <i>Y</i> axis
<i>E</i>	4.17e	Local torsional mode along <i>Z</i> axis
<i>F</i>	4.17f	Local bending mode along <i>Z</i> axis
<i>G</i>	4.17g	Local bending mode along <i>Y</i> axis
<i>H</i>	4.17h	Local bending mode along <i>X</i> axis
<i>I</i>	4.17i	Local bending mode along <i>Y</i> axis
<i>J</i>	4.17j	Local torsional mode along <i>Y</i> axis

Table 4.2: Steel core modes

most prominent on the graph on Figure 4.9 with the results obtained from the LE model. In particular all the modes besides the first intersect the second curve. This information with the prevalence of bending modes on those points lead to

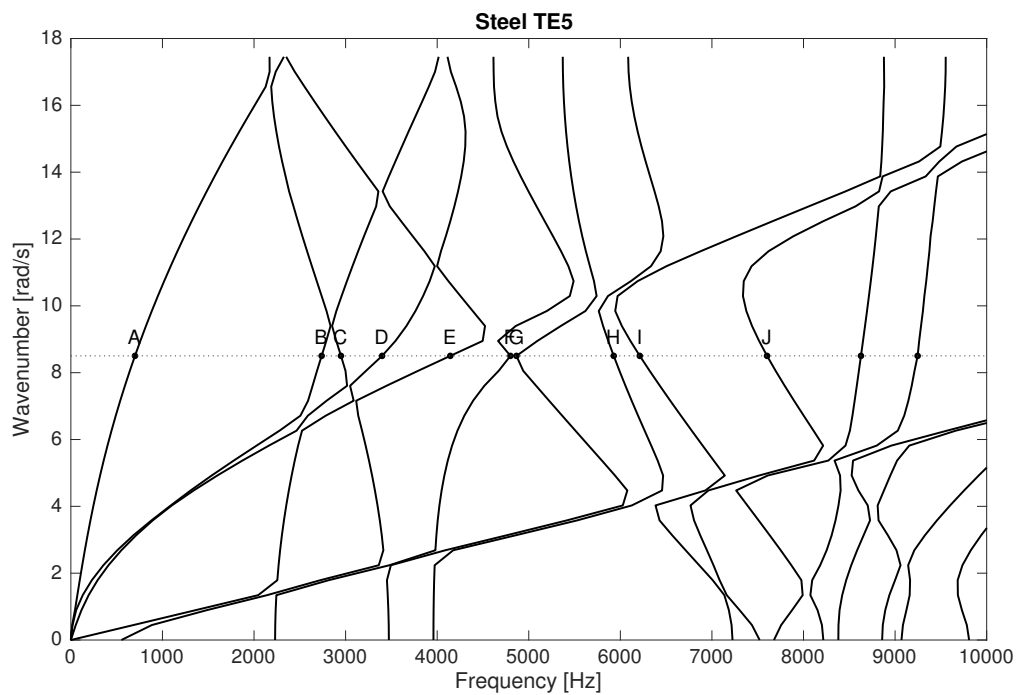
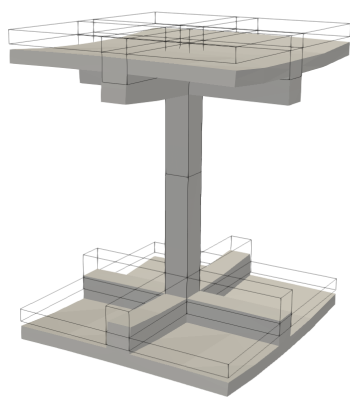
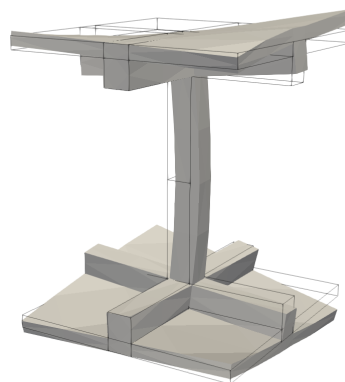


Figure 4.16: Steel modes reference graph



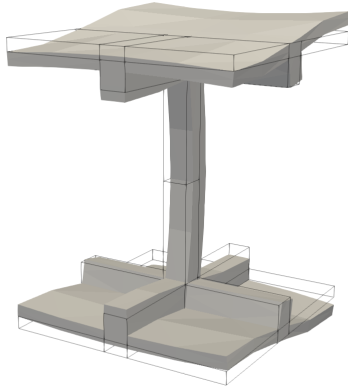
(a) Mode A



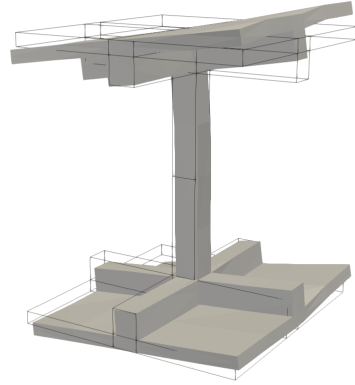
(b) Mode B

assume that this second curve represents a bending modes too.

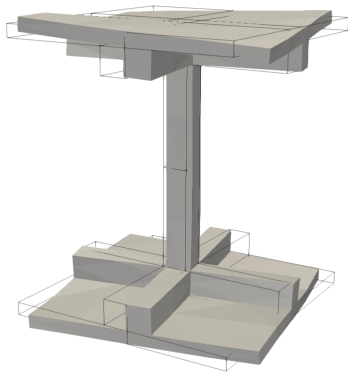
On Figure 4.18 the second configurations are presented. Contrary to the others options, on this one the same material of the plates is used for the core obtaining an homogeneous structure. This plain aluminium structure wasn't deeply analysed



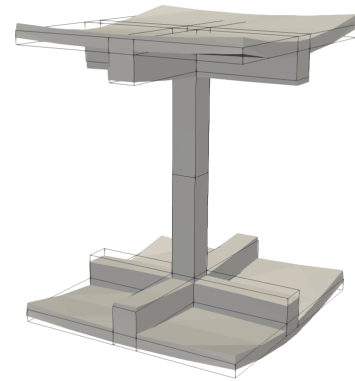
(c) Mode C



(d) Mode D

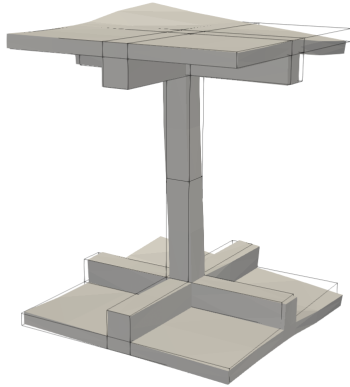


(e) Mode E

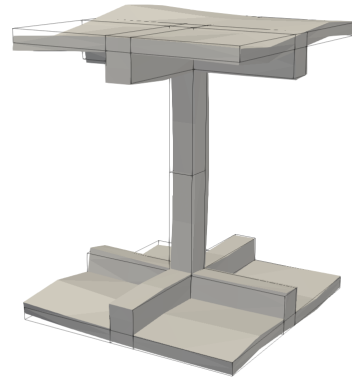


(f) Mode F

as the other two configurations previously on this chapter. Indeed it was mostly used as comparison for the other analysis, however this paragraph will cover its analysis. Regarding the modes of the structures, their trend is similar to the one already seen on the steel results on Figure 4.16: two curves, one rectilinear and one parabolic. But with this configuration both the curves are less defined and they are prone to dissipate with frequencies above 5000 Hz. The difference between the two configurations makes the last five modes of particular interest, especially modes F , G and H regarding the upper curve and modes I and J in relation to



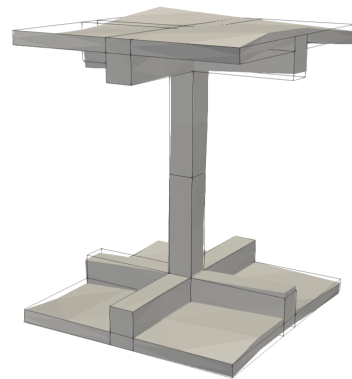
(g) Mode G



(h) Mode H



(i) Mode I



(j) Mode J

Figure 4.17: Steel modes illustration

the lower one.

Figure 4.19 contains the first ten modes from the analysis of the aluminium core model. As well as the previous illustration, also on this analysis the tridimensional models are superimposed with a wireframe to better track the deformation of the models. The axes used for the description of each mode are the same as the ones used on the steel core analysis: X axis from right to left of the page; Y axis pointing

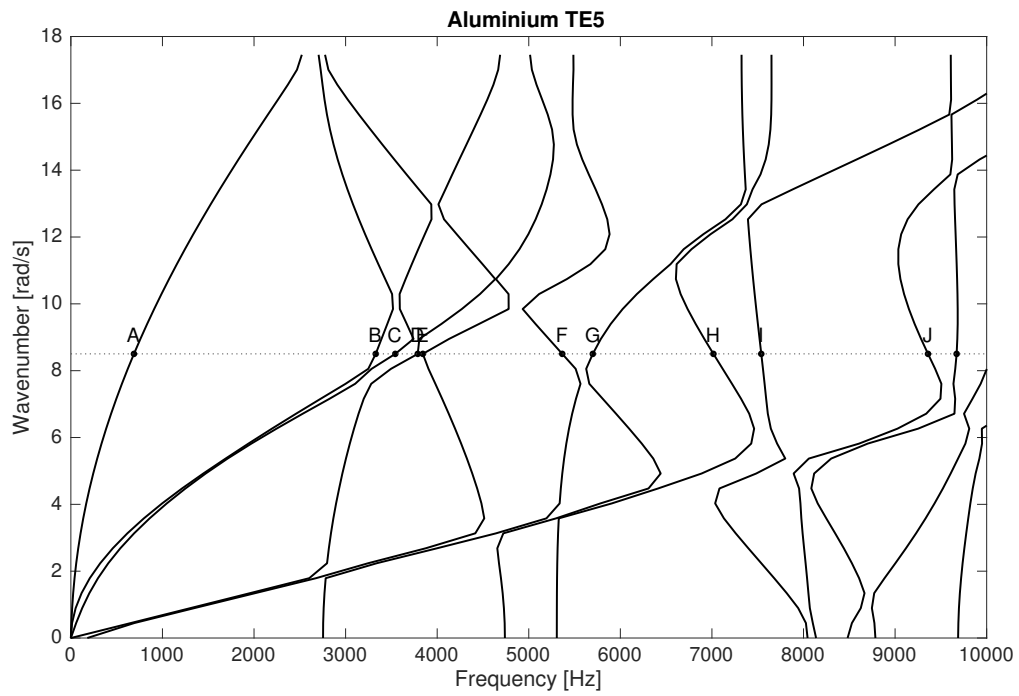
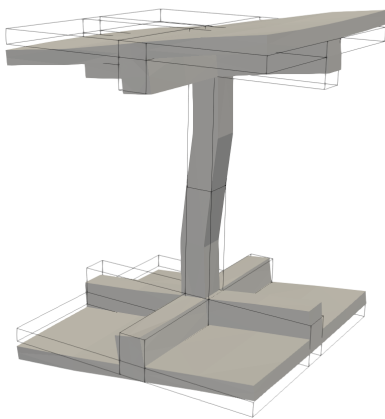
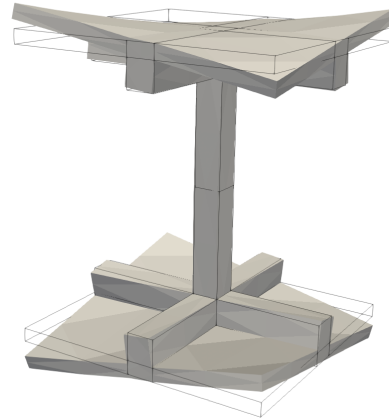


Figure 4.18: Aluminium modes reference graph



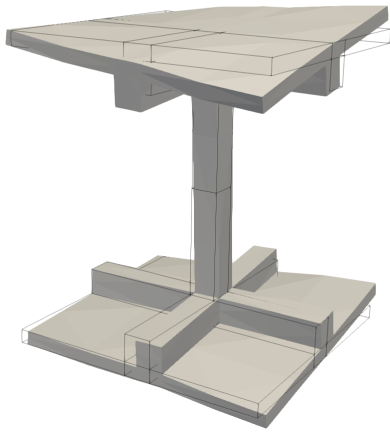
(a) Mode *A*



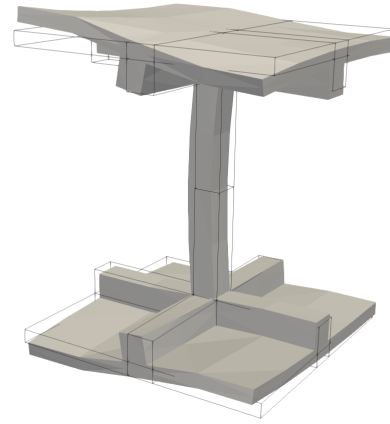
(b) Mode *B*

into the page; Z axis pointing up. The modes are described on Table 4.3

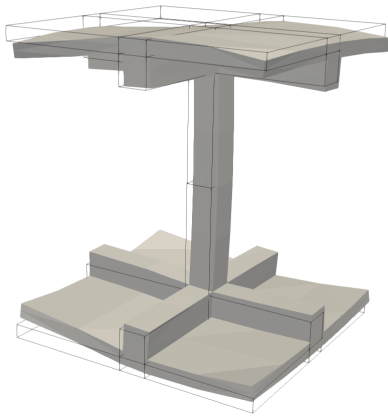
Likewise to the steel core results, most of the modes on this graph are bending ones with a handful of torsional modes. There are a lot of similarity between the modes, in particular: modes *G*, *H* and *J* share the deformation of the upper plates;



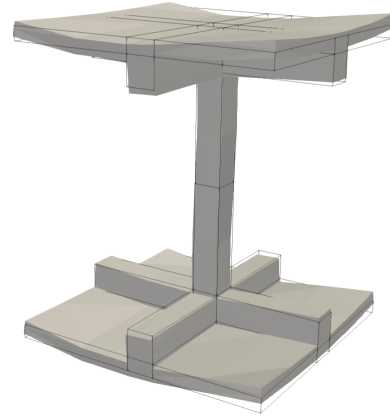
(c) Mode C



(d) Mode D



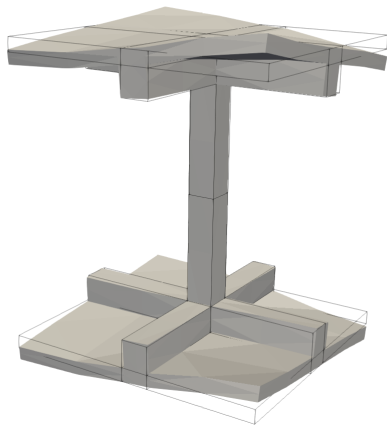
(e) Mode E



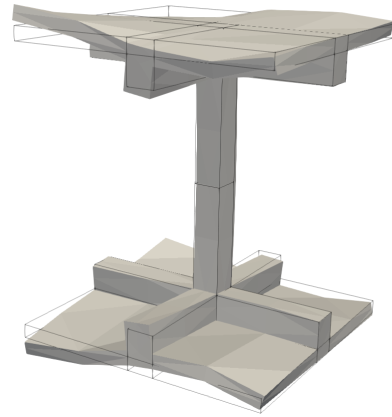
(f) Mode F

also modes E and F share the deformation of the same plates, but mirrored on the X-Y plane. These last two modes also share a similar distortion of the lower plates.

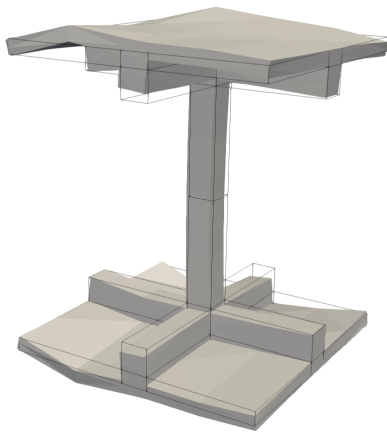
The last structure analysed is the aramid fibers core configuration, whose results are shown on Figure 4.20. Like the steel core ones, this configuration was deeply analysed on the previous sections due to the eye catching feature of this structure. The come back curve visible on the LE analysis results on Figure 4.11 and it is still visible on the later TE analysis on the fourth-order graph on Figure



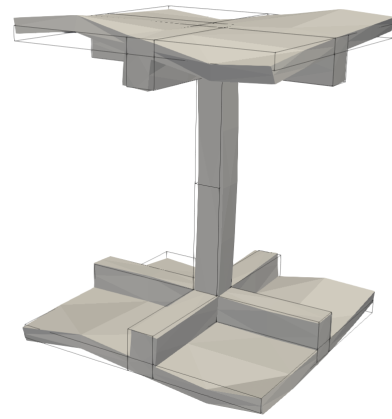
(g) Mode G



(h) Mode H



(i) Mode I



(j) Mode J

Figure 4.19: Aluminium modes illustration

4.15 is also noticeable on this last graph. In particular the curves where the modes D and E are extracted from are most likely the ones composing that feature. Also, the first two curves are of interest due to their straight intersection around 2000 Hz.

The ten modes from the dotted line on Figure 4.20 are represented on Figure 4.21. On this figure the modes are still represented as their tridimensional deformed

Mode	ref	Description
<i>A</i>	4.19a	Local torsional mode along X axis
<i>B</i>	4.19b	Local bending mode along Y axis
<i>C</i>	4.19c	Global bending mode along Y axis
<i>D</i>	4.19d	Global bending mode along X axis
<i>E</i>	4.19e	Local bending mode along Y axis
<i>F</i>	4.19f	Global bending mode along X axis
<i>G</i>	4.19g	Global torsional mode along Y axis
<i>H</i>	4.19h	Global bending mode along Y axis
<i>I</i>	4.19i	Global bending mode along X axis
<i>J</i>	4.19j	Global bending mode along X axis

Table 4.3: Aluminium core modes

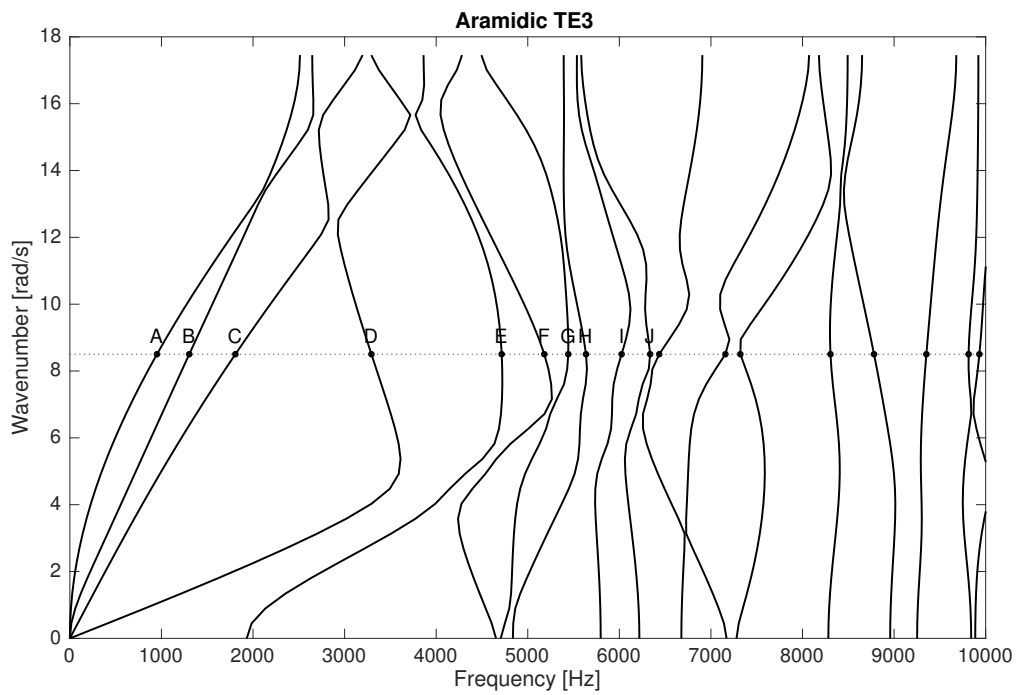
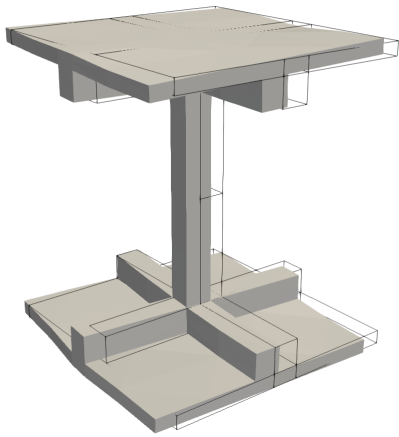
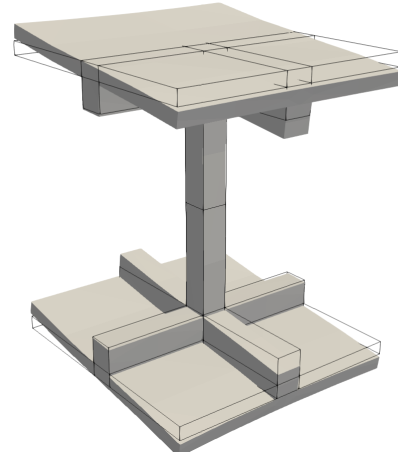


Figure 4.20: Aramidic modes reference graph

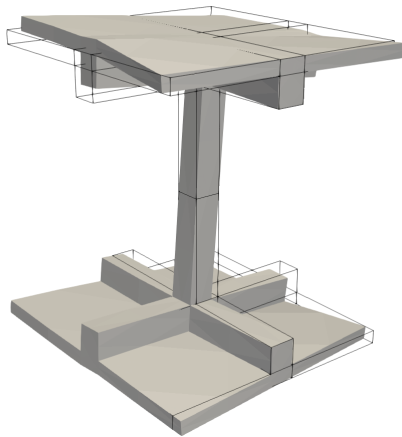
model with a superimposed wireframe of the original one as reference. Likewise the previous two analyses, the axes used for the description of each mode are: X axis from right to left of the page; Y axis pointing into the page; Z axis pointing up. The modes are described on Table 4.4



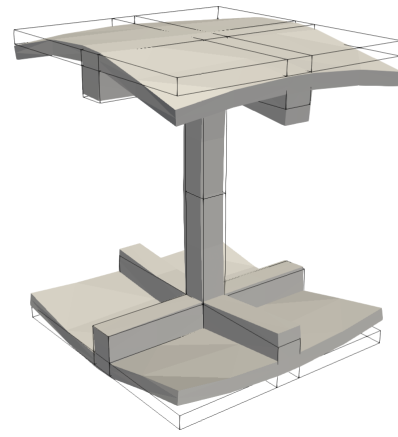
(a) Mode *A*



(b) Mode *B*

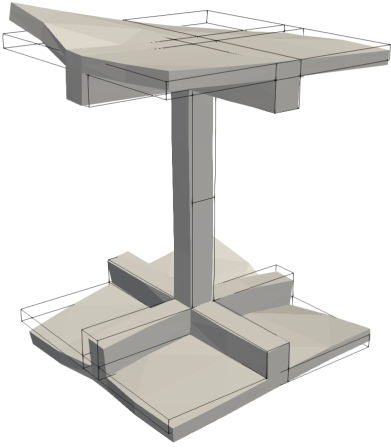


(c) Mode *C*

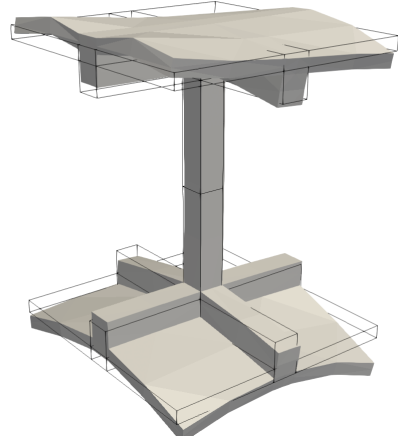


(d) Mode *D*

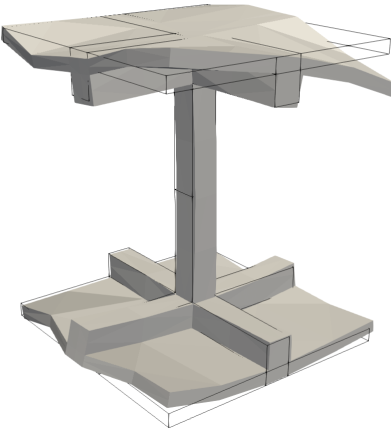
Also like the previous analysis, this case modes are most bending ones with just three torsional ones. In contrast with the previous configurations, the variety of modes is higher on this analysis and only a handful of modes are similar to the ones on the other configurations. Regarding the similarity of the modes within the aramidic fibers configuration: modes *F*, *H* and *J* have similar upper plates deformation, but only *H* and *J* share a similar lower plates strain while mode *F* have a similar lower plate to the mode *D* one, but mirrored on the X-Y plane; mode *A* and especially mode *B* have an almost rigid deformation.



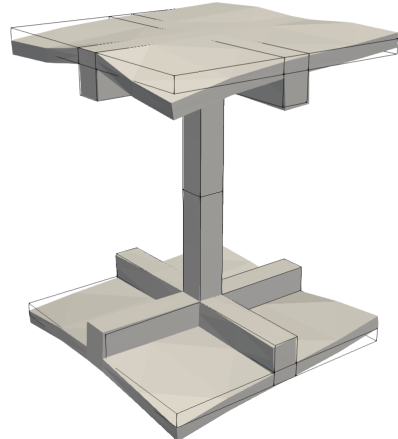
(e) Mode E



(f) Mode F



(g) Mode G



(h) Mode H

Part III

Conclusions

Conclusions

4.3 Characterisation

On the first chapters of this dissertation, it is analysed the characterisation of a cell. Firstly the geometric properties of the cell are analysed, in particular various types of Lagrange Expansion are tested to identify the best ones to balance accuracy and complexity of future simulations. By modifying both density of the mesh and type of cells, a comparative graph is crafted with the aid of this graph a 14L16 configuration is chosen as optimal. To accommodate the flexibility needed to link the single structure one to another, two more mesh cells are added to the mesh on the extremities of the gate. Besides the mesh optimisation, shear locking is taken into account during this chapter. In particular, algorithms for the mitigation of this phenomenon were tested. In conclusion, the effect of MITC algorithm on the performance of the simulation was marginal. Also, during this optimisation three alternative configurations were proposed.

Afterward, the effect on the performance of the materials used for the structure is explored. The selection of materials to be used on the simulations is done taking into account both obtaining a large range of properties and the opportunity to use this material with an Addictive Manufacturing process. This last trait is also in question when choosing the combinations between materials that will later be tested. Among the resulting combinations: two are single materials and they are used as baseline for the others; two are metal on metal with the same titanium alloy, but with reversed placement of the materials; last two are a metal on ceramic combinations where the high differences between the materials properties can highlight the importance of the materials choice on the performance of the

structures. The simulations done with these combinations lead to the identification of the optimal ones. In this case "optimal" means that with these combinations of materials the result varied more with respect to the baseline.

This combination is used for the next batch of simulations where the positioning of the materials on the structure is tested. During the second batch of simulations four configurations are identified by placing the two materials on different areas of the structure and within these configurations various symmetry are considered. A fifth configuration with randomised positioning of the materials is used as baseline for the comparison. To accommodate the need for bigger structures a 2X2 array of basic cells is used for the simulations instead of a simpler 1X1.

4.4 Wave propagation problem

During the first part of the document the results are obtained by solving an eigenproblem on the stiffness matrix obtained from the CUF package. This solution allows to study the behaviour of a structure when excited with various frequencies, this technique only allows the study of the modeled structure, which lead to more and more complex structures built from the combination of simpler cells. During the first part of this thesis this need to study bigger structures lead to the creation of different size models, like the 2X2 configuration used for the material positioning analysis. However, through the second part of this thesis a newer method is used.

The solution of the wave propagation problem lead to the understanding of the energy transfer mechanism inside a structure. One particular method for solving this kind of problems also allows to propagate the structure through one or two directions. This method, called Wave Finite Element Method (WFEM), is extensively used within the second part of this document to broaden the information obtainable from every structure. However, before starting to analysing our structure, a wide range of cases taken from other publications are studied with this method to compare the results acquired from the implemented code with the ones from the reference papers.

Afterwards, a new basic structure is proposed to make better use of the WFEM propagating capability, then this new geometry is used as core for a sandwich plate.

The analysis for this last iteration includes both discretisations with Lagrange and Taylor expansions, in particular for the TE various order of expansion are used from first-order to fifth-order. The sandwich structure is fitted with three different materials (steel, aluminium and aramidic fibers) on the core to study the performance of each configuration and compare them. The comparison is made firstly with the Lagrange expansion and afterward with the Taylor one. This last discretisation is the one used for the mode analysis. The first ten modes of each configuration are extracted from the Taylor analysis and compared between each other, both inside the same configuration and between the three configurations.

Bibliography

- [1] Clint Atwood et al. “Laser engineered net shaping (LENS™): A tool for direct fabrication of metal parts”. In: 1.1998 (2018), E1–E7. DOI: 10.2351/1.5059147.
- [2] Amit Bandyopadhyay and Bryan Heer. “Additive manufacturing of multi-material structures”. In: *Materials Science and Engineering R: Reports* 129. March (2018), pp. 1–16. ISSN: 0927796X. DOI: 10.1016/j.mser.2018.04.001. URL: <https://doi.org/10.1016/j.mser.2018.04.001>.
- [3] Erasmo Carrera et al. *Finite element analysis of structures through unified formulation*. Wiley, 2014. ISBN: 9781119941217. DOI: 10.1002/9781118536643.
- [4] Ken Cooper. “Microgravity Manufacturing: Extending Rapid Prototyping Past the Horizon”. In: *5th Conference on Aerospace Materials, Processes, and Environmental Technology* (2003). URL: <http://hdl.handle.net/2060/20040084023>.
- [5] Vincenzo D’Alessandro. *Investigation and Assessment of the wave and finite element method for structural waveguides*. 2014.
- [6] Matteo Filippi, Alfonso Pagani, and Erasmo Carrera. “High-order finite beam elements for propagation analyses of arbitrary-shaped one-dimensional waveguides”. In: *Mechanics of Advanced Materials and Structures* 0.0 (2020), pp. 1–9. ISSN: 15376532. DOI: 10.1080/15376494.2020.1842951. URL: <https://doi.org/10.1080/15376494.2020.1842951>.
- [7] Mark Helou and Sami Kara. “Design, analysis and manufacturing of lattice structures: An overview”. In: *International Journal of Computer Integrated Manufacturing* 31.3 (2018), pp. 243–261. ISSN: 13623052. DOI: 10.1080/

0951192X . 2017 . 1407456. URL: <https://doi.org/10.1080/0951192X.2017.1407456>.

- [8] Hongwei Sun, Xingwen Du, and P. Frank Pai. “Theory of metamaterial beams for broadband vibration absorption”. In: *Journal of Intelligent Material Systems and Structures* 21.11 (2010), pp. 1085–1101. ISSN: 1045389X. DOI: 10.1177/1045389X10375637.
- [9] S. Timorian et al. “Spectral analysis and structural response of periodic and quasi-periodic beams”. In: *Proceedings of the Institution of Mechanical Engineers, Part C: Journal of Mechanical Engineering Science* 233.23-24 (2019), pp. 7498–7512. ISSN: 20412983. DOI: 10.1177/0954406219888948. URL: <https://doi.org/10.1177/0954406219888948>.